Development of Nanohole-Based Sensors for Early Detection of Ovarian Cancer

by

Yu-Wei (Andrew) Chou
B.Sc., Simon Fraser University, 2008

A Thesis Submitted in Partial Fulfillment
of the Requirements for the Degree of

MASTER OF SCIENCE

in the Department of Chemistry

Supervisory Committee

Development of Nanohole-Based Sensors for Early Detection of Ovarian Cancer

by

Yu-Wei (Andrew) Chou
B.Sc., Simon Fraser University, 2008

Supervisory Committee

Dr. Alexandre G. Brolo, (Department of Chemistry)
Co-Supervisor

Dr. David Sinton, (Department of Mechanical Engineering)
Co-Supervisor

Dr. Cornelia Bohne, (Department of Chemistry)
Departmental Member

Abstract

Supervisory Committee
Dr. Alexandre G. Brolo, (Department of Chemistry)
Co-Supervisor
Dr. David Sinton, (Department of Mechanical Engineering)
Co-Supervisor
Dr. Cornelia Bohne, (Department of Chemistry)
Departmental Member

Ovarian cancer has very high mortality because it is hard to diagnosis in early stages. Many ovarian cancer biomarkers (such as HE4, CA 125) are available and had been suggested as potential tools for early cancer detection. However, early cancer detection using serological markers will only become widely used if a new generation of sensors that can be handled in a clinical setting can be developed. A detection technology that is promising for miniaturization and integration in biomedical sensing devices is based on the phenomenon of the extraordinary light transmission (EOT) through arrays of nanoholes on metal films. EOT is an increase in light transmission observed at certain wavelengths that satisfy the surface plasmon resonance (SPR) condition of the nanostructure. The position of this resonance is affected by surface adsorption phenomenon, which is the basis for the biosensor. In this dissertation, the detection of the HE4 biomarker was demonstrated using EOT. The EOT-based detection was compared to two state-of-the-art analytical methods (ELISA and commercial SPR). Based on our experiments, it was found that ELISA has lowest detection limit, around 0.5 ng/mL for that particular protein (HE4). The detection limits for the commercial SPR, around 0.13 μg/mL was comparable to the nanohole-based detection limit, around 1.76 μg/mL. In contrast to ELISA, the SPR-based methods were label free, more time efficient, and more

environmental friendly. An extra advantage of the nanohole scheme was that multiple samples could be analyzed simultaneously and in real time. Adsorption kinetic experiments were also performed to evaluate the rate constants of the HE4 binding to a surface coated with anti-HE4. The adsorption equilibrium constant for the HE4 – anti-HE4 system was determined to be $(4.3 \pm 2.1) \times 10^{7}\ M^{-1}$.

Table of Contents

List of Tables

List of Figures

List of Abbreviations

BCCA	British Columbia cancer agency
BSA	Bovine serum albumin
CCD	Charged-coupled device
CT	Computed tomography
DMSO	Dimethyl sulfoxide
DSU	Dithiobis(succinimidyl undecanoate)
ELISA	Enzyme linked immunosorbent assay
EOT	Extraordinary optical transmission
FIB	Focused ion beam
FTIR	Fourier transform infrared spectroscopy
HE4	Human epididymis protein 4
LD	Lower detection limit
LED	Light-emitting diode
MRI	Magnetic resonance imaging
PBS	Phosphate buffered saline
PDMS	Polydimethylsiloxane
PET	Positron emission tomography
RU	Response unit
SEM	Scanning electron microscope
SERS	Surface-enhanced Raman scattering
SPR	Surface plasmon resonance
Strep-AP	Streptavidin-alkaline phosphatase
TBST	Tris buffered saline + 0.1% Tween 20

Acknowledgments

I would like to thanks to many people and groups. The greatest thanks to my supervisor, Alexandre Brolo, who guided and assisted me on my research. I would also like to thanks all other past and present group members, Dr. David Sinton and Dr. Reuven Gordon and their group members for always giving me good suggestions and great help on microfludic support; Carlos Escobedo for microfludic and PDMS channel designing and making; Dr. Xiabo Duan and his groups from BC Cancer Agency for technical help on ELISA and Biacore-SPR; Hao Tang for kinetic calculation help; Mohammad Rahman for nanohole array sample fabrication; many other individuals who I cannot mention all in here.

Chapter One: Introduction

1.1 Objective

1.1.1 Ultimate Goal

The ultimate goal of this research is to help on the development of a label free biosensor capable of detect (ovarian) cancer markers from physiological fluids, such as blood or serum, in the early stages of the disease. The idea is to produce a cheap device that can provide a quick response in clinical settings[1-3] for point of care screening. An idealized flow chart for cancer diagnosis process based on this device is presented in Figure 1-1.

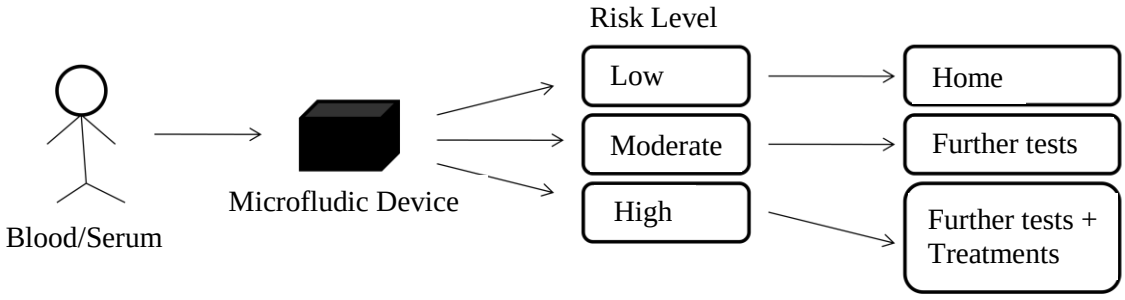

Figure 1-1: Scheme diagram of the microfludic device.

In an ideal scenario, blood samples are collected from patients directly in a clinic. The raw blood sample is introduced into a miniaturized device that contains a microfluidic system and a biosensor[4,5]. The sample preparation is done within the microfluidic system[6]. The worked up sample is then introduced in a detection chamber, containing an internal calibration, where the level of a certain number of proteins previously linked to the ovarian cancer will be quantified. All these proteins should be detected simultaneously. Based on the concentration level of these biomarkers in the

history of the patient, the outcome of the screening would be classified in risk levels (low, moderate, or high). Based on these results, the clinician can decide the appropriate response. The patients considered low risk can be release without further testing after the screening, while patients with high-risk might be rushed to either initiate treatment or further, more comprehensive, examinations[7]. The ideal device should be small, portable, and easy to use in order to be useful in providing the required screening of a large number of patients, as suggested above.

1.1.2 Thesis Goal

In order to progress towards the ultimate goal outlined in section 1.1.1, our research group and collaborators had been working on a new sensing technology based on the optical properties of arrays of nanoholes on Au thin films. This detection scheme is based on the excitation of surface plasmon resonances (SPR) that enable the enhanced transmission of light at certain conditions. Proof of concept experiments on the application of nanohole arrays for the detection of proteins in either in "flow-over"[8-12] or "flow-through"[13-15] configurations have been reported. In this thesis, we performed a head-to-head comparison of this new technology, biosensing based on nanohole arrays, with a couple of biosensing methodologies that are available commercially (ELISA and Biacore-SPR) for an ovarian cancer biomarker assay. The analytical methods were evaluated in terms of sensitivity, detection limit, and speed of detection. We also aimed at determining the binding constant of the ovarian cancer marker and at developing a dilution microchip that can potentially provide an on-site calibration for the protein of interest.

1.2 Why Ovarian Cancer?

Although the cancer screening device should work for any type of cancer that can be diagnostic through serological testing, ovarian cancer was chosen as our first strategic target. This is because ovarian cancer has a high mortality worldwide because it is very hard to diagnose in early stages[16]. Ovarian cancer is the fifth leading cancer death cause among women in the United States, being the gynaecological cancer with highest death rate[17]. Based on estimations from the American Cancer Society, there will be 21,880 new cases of ovarian cancer diagnostics and 13,850 deaths in the United State in 2010[17].

Ovarian cancer is very hard to diagnosis in early stages because their symptoms are unspecific and vague[18]; therefore, they are easy to be ignored or missed. The five-year survival rate is greater than 90% when ovarian cancer is found at early stages and patients are given a proper treatment. This rate drops to only 20 to 30% when the cancer is found at a later stage[19].

1.2.1 Diagnosis of Ovarian Cancer – State-of-the-art

The common tests currently used in ovarian cancer diagnostics are pelvic exam, transvaginal ultrasound, CA125 test, computed tomography (CT) scan, positron emission tomography (PET) scan, and magnetic resonance imaging (MRI). Although there exist several different methods for ovarian cancer diagnostic, there is no single test that can reliably detect ovarian cancer in early stages[20].

The pelvic exam and transvaginal ultrasound are not specific for ovarian cancer[21]. The pelvic exam is generally a test which is used to determine any type of pelvic problem. Several different diseases from uterus, fallopian tubes, or ovaries can cause pelvic problems. All the image scanning methods, CT, PET, and MRI, are complex, require very experienced doctors, and are not suitable for early stage screening.

The CA-125 test is the most widely used serological test for early ovarian cancer diagnostic or screening the treatment of ovarian cancer[22,23]. A high (or rising) level of CA-125 can indicate that the patients have the corresponding disease (e.g. ovarian cancer) or that the disease has recurred. This test is based on the enzyme linked immunosorbent assay (ELISA) and the intensity of the fluorescence signal is related to the level of CA-125 in blood. The principles of ELISA will be introduced in chapter 3.2.1. In general, the normal level of the CA-125 in a healthy women is below 35 Units/mL[22,23].

The CA-125 is an ovarian cancer marker found by Bast, Knapp, and their group in 1981[16]. Although the level of CA-125, a protein found in blood, can be correlated to the presence of ovarian cancer in the early stages, the test is unreliable in many cases because there are many other factors that affect the levels of CA-125. These factors include other type of cancers, benign conditions or disease in other areas, such as endometrium, fallopian tubes, lungs, breast, and gastrointestinal tract[24]. In some case, even pregnancy[25] can affect the levels of CA-125. In practice, only 50% of true positives are detected in

early stages, the other half are either false positives or false negatives. Therefore, extra care must be taken on the interpretation of CA-125 tests, and it can only be considered as initial step towards the proper diagnostic[26]. A procedure to solve this reliability problem is to perform regular CA-125 tests in the same patient. In this way, CA-125 levels for a given patient are monitored with time to generate a baseline and avoid the effect of other factors on the CA-125 level in a short term. Even considering the expenses related to regular testing, this type of approach could be very cost effective. For instance, a recent study shows that about 40% reduction in ovarian cancer mortality would lead to an extra US $73,469 dollars per year life save (base case) and $36,025 per year life save (high-risk population)[27]. This cost recovering was estimated considering 12 months screening interval, but in order to reduce the mortality above 50%, screening intervals less than 12 months may be needed[27]. Another important point is that the screening should be performed for several different biomarkers. That would provide a better overview of the patient health and lead to more cost saving, since other diseases could also be diagnosed. This type of regular screening would require a cheap analytical platform capable of multiplex detection of several proteins in real time.

1.3 Biomarkers

In general, biomarkers are substances that are used to indicate certain biological states. In our case, the biomarkers are the proteins produced by the ovarian cancer cell and we can use them to diagnosis ovarian cancer. There are multiple biomarkers for the ovarian cancer such as CA-125, HE4, MUC16, MSLN, MMP7[19,28]. In this thesis, only HE4 was studied using three methods for comparison. In future works, more biomarkers

could be studied using similar methodology that developed in this thesis. Furthermore, multiple biomarkers could be run at the same time in the same sensor chip in order to reach the global overview of the levels of several species simultaneously.

1.3.1 HE4

The HE4 antigen is the ovarian cancer biomarker used in this thesis. It is also called WFDC2, MGC57520, and WAP5[29,30]. It is a human gene located in the chromosome 20. It consists of 124 amino acids and is 12993 a.m.u[29,30]. The sample used in this study was provided by Dr. Xiaobo Duan from the British Columbia Cancer Agency (BCCA) Vancouver Island Centre and the molecular weight was around 11,000 a.m.u.

1.4 Structure of this thesis

This thesis is divided into six chapters. Chapter one is the introduction chapter where the motivation and the goals of the thesis were delineated. Chapter two deals with the theory for SPR. This provides the theoretical foundation of our main research technique. Chapter three shows the experiment detail and results about commercial methods (ELISA and Biacore) for HE4 analysis. Chapter four shows experiment details and results of the nanohole SPR. Chapter five shows the approach for calculating association and dissociation constant. All results for each method were summarized in chapter six.

Chapter Two: Surface Plasmon Resonance

2.1 Surface Plasmon Resonance (SPR)

2.1.1 History

Surface plasmon was first observed by Wood in 1902[31]. Wood took the spectra of a metal grating using an incandescent lamp. At the time, the spectral observation were not explained clearly and Wood referred to them as a "sharp and black peak" in the spectrum[31]. Almost 40 years later, Fano linked Wood's observations to electromagnetic waves propagating on metallic surfaces[32]. In 1958, Thurbadar observed a large reflectivity drop on thin metal films and Otto explained it as surface plasmon in 1968[33]. In Otto's experiment, the light was directed through a prism on a metal (silver) surface with a small gap between the prism and the metal; and surface plasmon resonance was excited on the metal surface. Kretschmann and Raether establish a new configuration to excite surface plasmon at the same year. In Kretschmann's setup, there were no gap between the prism and the metal. Instead of the small gap, a very thin metal film was deposited on a supporting substrate (glass) and the surface plasmon resonance was excited from the other side of the metal surface. This configuration, now called Kretschmann-Raether configuration, is the most used arrangement in the current generation of commercial SPR systems[34]. In the 1970s, surface plasmon resonance was wildly used in metal surface studies and to the determination of metal thickness. The first commercial SPR-based sensor (Biacore) was produced in 1990 for the studies of the

interaction between biomolecules. After that, SPR techniques have been used greatly in many fields[35,36].

2.1.2 Acquiring SPR data

Surface plasmon resonance (SPR) is a phenomenon that can be observed on a gold surface when certain conditions (Chapter 2.1.3) are met[37]. SPR manifest as a huge drop on reflectivity of a monochromatic incident radiation observed at a certain angle. This angle is called surface plasmon resonance angle (SPR angle). The SPR angle is very sensitive to the refractive index at the surface of the gold film. Therefore, the SPR angle changes when the refractive index at the gold surface changes.

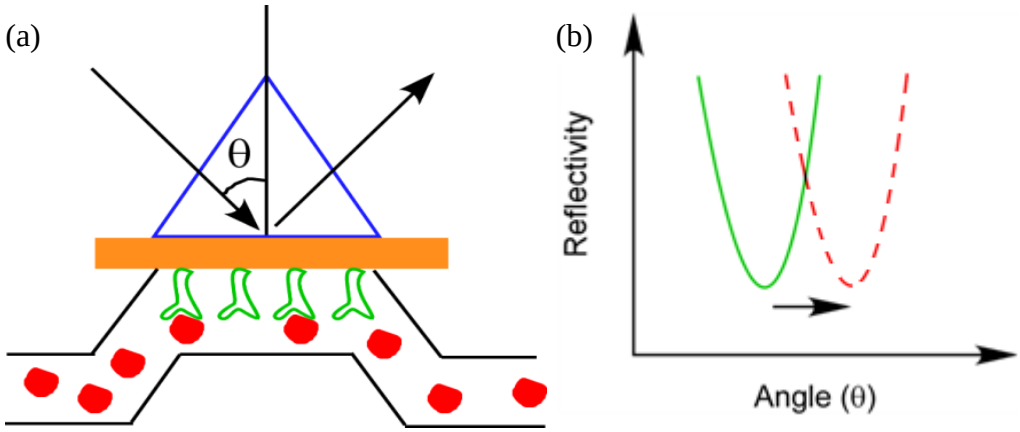

Figure 2-1: a) Schematic representation of an SPR biosensing experiment using the Krestchman-Raether configuration. The green objects represent antibodies immobilized at the gold surface (orange) and the red circles are antigens in a microfluidic channels; b) SPR reflectivity curve before (green-solid line) and after (red-dash line) binding.

In standard biosensing measurement, the refractive index on the gold surface changes when proteins adsorb to the surface. As shown in Figure 2-1, when an antibody is attached to the gold surface and the complementary antigen is present in the solution, the interaction between the pair leads to changes in the refractive index at the surface (Figure 2-1a), resulting in a SPR angle shift to higher angle values[37] (Figure 2-1b).

In commercial SPR systems, the system detects the SPR angle shifts and converts it to a response unit (RU) change. In the particular case of the Biacore system (the most common commercial SPR in the market), 1000 RU is equal to ~ 0.1^{o} of SPR angle change[38]. The RU values can be plotted against time during the course of a binding experiment, as shown schematically in Figure 2-2, in order to provide kinetic curves. These curves can be used to extract information regarding the protein-protein interaction, including the affinity constant[39].

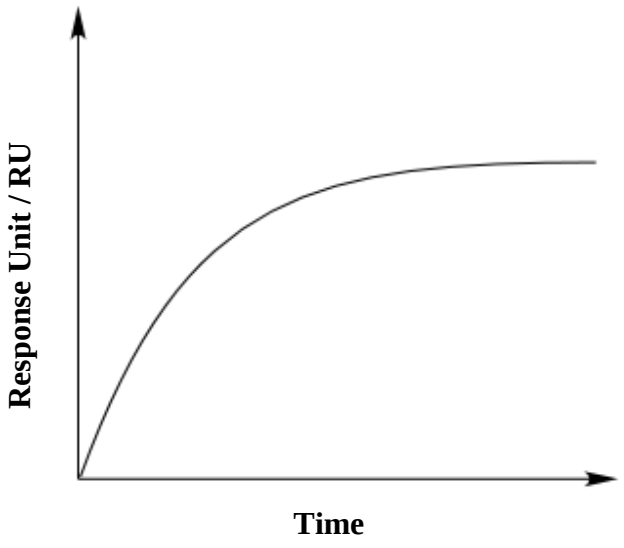

Figure 2-2: Schematic diagram of an affinity kinetic plot obtained using a Biacore-SPR system.

2.1.3 SPR Conditions

In the previous section (2.1.2), we concentrated the discussion on a general description of the SPR experiment for biomolecular sensing and on the type of information that can be obtained from those measurements. Here we will discuss the details of the light – SP coupling mechanisms. Two type of coupling will be discussed: prism-coupling and grating-coupling.

2.1.4 Prism Coupling

The first coupling condition is based on the Kretschmann configuration which is part of the commercial Biacore system. The Biacore is the system used in our experiments presented in Chapter 2. For a particular frequency, SPR will only be excited when the parallel component of the incident light momentum (k_x) is matches the surface plasmon momentums (k_{sp}) (Figure 2-3)[37]. This condition can never be satisfied for light incident directly to the metal surface, but in the Kretschmann configuration, the momentum matching condition is achieved by prism-coupling through a thin gold film[40]. Typically, the thickness of the metal film is around 50 nm[40].

As shown in Figure 2-3, the parallel component of the momentum of the incident light can be expressed as equation 2-1 and the surface plasmon momentum can be calculated based on the dielectric constant of two interface layers (metal and dielectric) and the momentum of the incident light (equation 2-2)[37]. For all incident angles, the SP

momentum at the glass-gold interface ($k_{sp\ glass\text{-}gold}$) is always greater than $k_{x\ glass}$ (light incident through the prism). Since there two momenta do not match, SPR cannot be excited in the glass-gold interface.

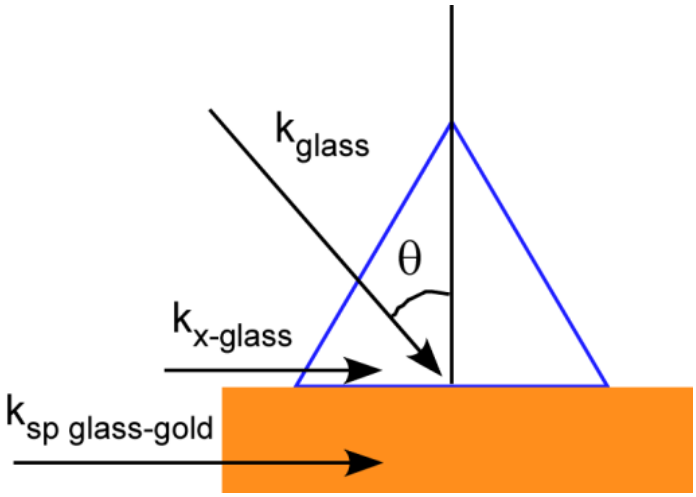

Figure 2-3: Schematic representation of the momenta in the gold – glass interface for a Kretschmann configuration. As discussed in the text, surface plasmon resonance cannot be generated on glass-gold interface because the momentum matching condition is not satisfied.

$$k_{x-glass} = k_{glass} \sin\theta \tag{2-1}$$

$$k_{SP(glass-gold)} = k_{glass} \sqrt{\frac{\varepsilon_{glass}\varepsilon_{gold}}{\varepsilon_{glass} + \varepsilon_{gold}}} \tag{2-2}$$

In the case shown above, it seems that SPR can never be excited, but SPR is observed in practice. As we discussed above, SPR could not be excited on the glass-gold interface. However, when the incident angle is greater than the critical angle, an evanescent wave is created that can propagate through the thin gold film and excited

SPR[37] on the gold-air interface. In this case, surface plasmon momentum at the gold-air interface is given by (equation 2-3).

$$k_{SP(gold-air)} = k_{air}\sqrt{\frac{\varepsilon_{gold}\varepsilon_{air}}{\varepsilon_{gold}+\varepsilon_{air}}} \qquad (2\text{-}3)$$

On the other hand, the evanescent wave carry the same character as the incident light which given by equation 2-1. In this case, the two momenta can be matched at certain angle and SPR can be excited on the gold-air side (Figure 2-4).

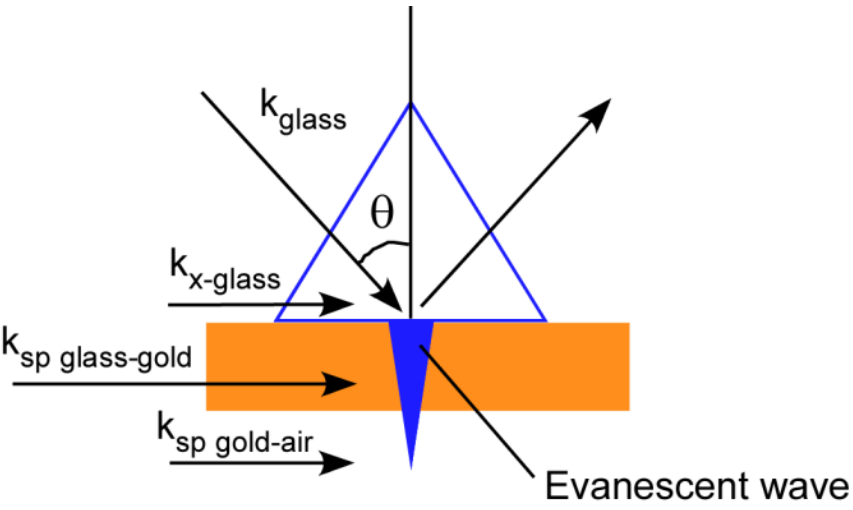

Figure 2-4: Schematic representation of the momenta in a simple prism-coupling surface plasmon resonance experiment generated on a gold-air interface (Kretschmann configuration). The evanescent filed, created due to total internal reflection, travels through the ~50 nm gold film and excite SPs at the gold – air interface.

This special angle is called SPR angle. As shown in equation 2-3, the value of $k_{sp\ gold\text{-}air}$ changes when ε_{air} is altered by, for instance, a surface adsorption event. This adsorption would then lead to a change in the SPR angle as presented in Figure 2-1b.

2.1.5 Grating Coupling

As discuss above, SPR can be generated by using the prism-coupling mechanism. SPR can also be created using a metallic grating. A metallic grating is fabricated by inscribing a periodic pattern on the gold (metal) surface[41]. This patterning can be well organized arrays of – metallic lines, nanoparticles, nanoholes, etc[14,42]. The SPR excited directly on a patterned gold film is generated by grating coupling[41]. Again, as we discuss in section 2.1.2, the parallel component of the incident light momentum (k_x) needs to be adjusted to match the surface plasmon momentum (k_{sp}) in order to generate SPR at a certain frequency. In the 1D grating case, the x component can be express as equation 2-4[43] :

$$k_x = \left(\frac{\omega}{c}\right)\sin\theta \pm \frac{2\pi}{\Lambda}m = k_{sp} \tag{2-4}$$

Where ω is angular frequency; c is speed of light in vacuum, m is an integer, Λ is periodicity of array. The periodicity is defined as feature-to-feature distance, as indicated in the Figure 2-5. As it can be seen in equation 2-4, the factor m provides multiple values for k_x vector and one of them would be able to match the surface plasmon momentum at a certain angle.

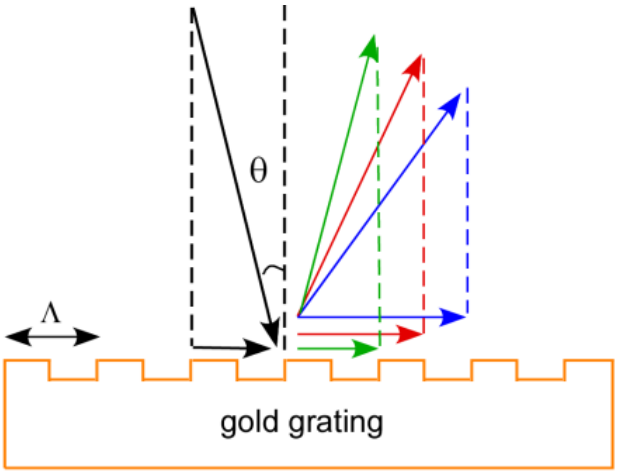

Figure 2-5: Schematic representation of surface plasmon resonance excited by grating coupling. The patterning of the gold surfaces creates different parallel-component vectors for the light momentum and one of them will match the surface plasmon momentum vector.

As shown in Figure 2-5, k_x can be changed based on the grating angle. Therefore, SPR can be excited without a prism. The periodicity can be changed in order to tune the wavelength range of the resonance condition.

2.2 Extraordinary optical transmission

Extraordinary optical transmission (EOT) is an enhancement in the transmitted light through subwavelength (diameter of nanohole is much smaller than wavelength of incident light) apertures observed at certain wavelengths. In 1944, Bethe show that the light transmission decreased with the ratio of radius of hole and wavelength to the power of four for a single hole on an infinitely thin and perfect metal[44]. In the real case, a metal always have some thickness. Therefore, the depth of hole gives the metal a waveguide property and the propagation of light inside the hole will need to be taken into consideration as well[45].

Based on Bethe's theory, practically no light should be transmitted through subwavelength apertures when the wavelength is about 3 times the diameter of the hole. However, a significant amount of light transmission is observed when arrays of nanoholes in gold or silver films are used. In 1998, Ebbesen notice that the amount of light transmitted through the arrays is even larger than the predicted light transmitted through an equivalent "big" hole formed by the sum of the areas of all the nanoholes in the array. This effect of increasing light transmission is due to surface plasmon resonance (grating coupling), as discussed before. As mentioned in section 2.1.4, SPR propagates parallel to the surface of the metal and this propagation distance is one of the characteristics that define the SPR waves. The SPR field is also confined to the metal surface, and it decays exponentially as the distance from metal surface increases[45].

2.2.1 Transmission Measurements: Different Configurations

In the section 2.1, we had shown that the reflected monochromatic light can be measured in SPR to detect the refractive index changes at the metal-dielectric interface. Other experimental configurations can be set to measure changes on different parameters (such as wavelength, intensity, and phase) due to surface adsorption. For instance, the white light transmitted through the arrays of nanoholes at normal incidence present peaks at certain wavelengths where the SPR conditions, given by equation 2-5 are satisfied

$$k_x = \left(\frac{\omega}{c}\right)\sin\theta \pm \frac{2\pi}{\Lambda}\sqrt{i^2 + j^2} = k_{sp} = \frac{2\pi}{\lambda}\sqrt{\frac{\varepsilon_{gold}\varepsilon_{air}}{\varepsilon_{gold} + \varepsilon_{air}}} \qquad (2\text{-}5)$$

Since the transmission light is at normal incident, the sinθ is equal to 0. Thus, the equation can then be further simplified to

$$\frac{2\pi}{\Lambda}\sqrt{i^2+j^2}=\frac{2\pi}{\lambda}\sqrt{\frac{\varepsilon_{gold}\varepsilon_{air}}{\varepsilon_{gold}+\varepsilon_{air}}} \quad (2\text{-}6)$$

After we rearrange the equation 2-6, the equation 2-7 can be obtained.

$$\lambda=\Lambda\frac{\sqrt{\frac{\varepsilon_{gold}\varepsilon_{air}}{\varepsilon_{gold}+\varepsilon_{air}}}}{\sqrt{i^2+j^2}} \quad (2\text{-}7)$$

Where λ is the wavelength transmitted through the array; Λ is the periodicity of array; ε_{gold} and ε_{air} represents dielectric constant of gold and air; i and j represent integers that define scattering order of the array along the x and y direction respectly. In the equation 2-7, we can see when the white light is used to transmitted the array the collected wavelength can be changed by changing the periodicity (Λ). Furthermore, when Equation 2-7 shows a fixed periodicity, the resonant transmitted wavelength will change to match the SPR conditions after surface adsorption.

2.3 Nanohole Arrays in Biosensing

Arrays of nanholes in metal films have been shown to be useful in several applications in the past decades. Besides biomolecular sensing[8,10-12], these devices were also used for surface-enhanced Raman scattering (SERS)[9], and for the enhancement on absorption spectroscopy[46].

The biosensing is the most important type of applications for this class of nanostructures. With the help of microfludic system, nanohole array with SPR effect result in a great approach in biomolecular sensing because of the advantage on real-time

sensing and small quantity of molecular implied. The transmission setup had been used in our group for studying the protein-protein binding by flowing over the interest protein on a modified gold surface. Compared to the prism coupling, the grating coupling provide possibly lower detection limit due to the small size of nanohole array. The flow through scheme was also proposed to further decrease the limit of detection[14]. In the flow through scheme, the interest protein is bound to the inner wall of the nanohole array rather than the surface of the gold plate[14]. In the case, the analytes adsorbed faster, due to the small cross-section, and they adsorbed on the region which had strongest SPR[15]. Other parameters (shape, size, and periodicity) of nano-structures are also studied to improve detection limit and sensitivity. Beside the flowing style and the ability to tailor the nanohole parameters, the grating coupling SPR also give us opportunity for real-time measurement of multiple arrays.

Chapter Three: Enzyme-Linked Immunosorbent Assay (ELISA) and Commercially Available SPR technology (Biacore)

In this thesis, the nanohole-based detection is compared to two other methods used to probe antibody-antigen interactions that are commonly used and are available commercially. These methods are the ELISA, and the SPR using Kretschmann geometry implemented by Biacore (Biacore-SPR). All the three methods were used to test against HE4 antibody and antigen binding. The three methods were compared in terms of sensitivity, detection limit, and speed of detection. Although the antibody-antigen binding might respond differently in each method, these comparisons were found to be a good guide to help improving our nanohole sensing technique. In this chapter, the experimental details and results of the ELISA and Biacore will be discussed. The details for the nanohole technique will be presented in Chapter 4.

3.1 Producing HE4 Antibodies

In order to detect a biomarker in blood, it is necessary to capture it specifically onto a sensing platform. This is achieved by using immobilized capturing antibodies. These antibodies are obtained by immunizing host animals, such as mouse, donkey, or rabbit with the biomarker of interest[48]. The immune system of the animal recognizes the biomarker as a foreign substance and produces antibodies that specifically bind to them. These antibodies are combinations of multiple biomolecules which are all able to recognize the same biomarker (antigen). This combination of biomolecules is called

polyclonal antibodies[48]. If only one kind of biomolecule was separated and cloned using hybridoma cells, this would be called a monoclonal antibody. In this thesis, all antibodies used were monoclonal[48]. The antibodies were specific to the HE4 protein (antigen) which is a biomarker for ovarian cancer[30].

3.2 Enzyme-Linked Immunosorbent Assay (ELISA)

3.2.1 Fundaments of the Method

Enzyme-linked immunosorbent assay (ELISA) is the most common used technique to detect antibody and antigen binding in biochemistry[49]. It is a powerful method able to determine ng/mL to pg/mL amounts of materials in solution. ELISA is realized using commercially available plates containing various numbers of wells as shown in the Figure 3-1.

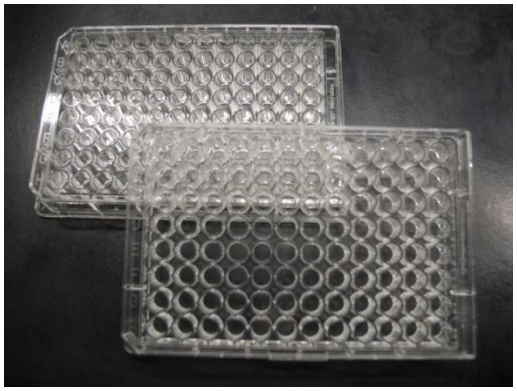

Figure 3-1: An image of commercially available ELISA plates (96 wells).

A scheme for a typical ELISA is shown in Figure 3-2. The container in Figure 3-2 represents one well of an ELISA plate (Figure 3-1). In general, there are 5 steps in an

ELISA[49]. The first step is the immobilization of target protein to the bottom of the well. Commercial ELISA plates are "activated" by an antigen with plate buffer (sodium carbonate buffer, pH=9.5) in the well in order to provide an appropriate target. The second step is to block the remaining of the well walls with bovine serum albumin (BSA) to prevent nonspecific binding. The first two steps were to generate the target for the antibody of interest. The third step is the binding of the antibody of interest to the immobilized antigen. Only the antibody that is specific to the immobilize antigen will recognize and bind to it. The last two steps are related to the quantification of the bounded antibody. The fourth step is then the binding of a secondary antibody for detection. The secondary antibody is "marked" with an enzyme. In the fifth and final step, a substrate (specific for the enzyme) is added to the well. The enzymes will catalyze the substrate decomposition, producing a fluorescent product that can be detected using a plate reader. The fluorescence intensity in this last step is proportional to the amount of antibody of interest captured in the assay.

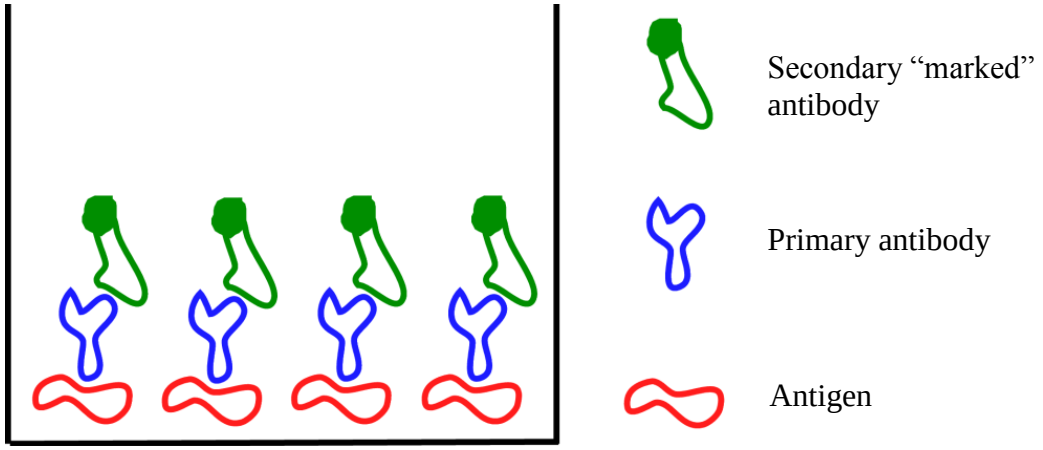

Figure 3-2: Schematic diagram of protein binding for ELISA.

ELISA assay is also available in sandwich format for experiments requiring better selectivity[49]. In the sandwich assay, the primary antibody is attached in the first step with a concentration that is high enough to coat most of the surface well. The target antigen is then introduced into the well and is captured by the primary antibody. After that, the second antibody (secondary antibody or detection antibody) is introduced. The secondary antibody is labelled by, for instance, a fluorescence probe. The interaction between the secondary antibody and the antigen is probed by the intensity of the fluorescence signal. In the regular ELISA, fault signal can be detected if the first antibody binds to any other proteins beside the target antigen. In the sandwich assay, both antibodies need to bind the antigen in order to provide the fluoresce signal. Therefore, the sandwich assay provides much better selectivity[50].

3.3 Biacore-SPR

Biacore is the company that released the first surface plasmon resonance (SPR)-based commercial sensing platform[37]. Many generations of Biacore machines (Biacore A100, Biacore X100, Biacore T200, Biacore 4000, etc) were developed in the last two decades[38]. It is a widely used platform to study protein binding characterization, drug discovery, and immunogenicity[51,52]. Protein characterization, protein-protein interactions and binding affinities are the main types of systems investigated with Biacore-SPR systems[53-56], due to the ability of the machine to perform real time measurement. Moreover, SPR is a “label free” method that depends only on the changes in the refractive index close to the surface. This is a definitive advantage over fluorescence-

based detection, such as ELISA, as native protein can be used without any modifications which might hinder their activity.

3.3.1 Biacore: Fundaments of the Method

In chapter two, section 2.2.1, we had discussed how SPR works. We will briefly reproduce some of that discussion here for clarity. The Biacore is a commercial machine that is based on the SPR technique. The principles of SPR are summarized in Figure 3-3.

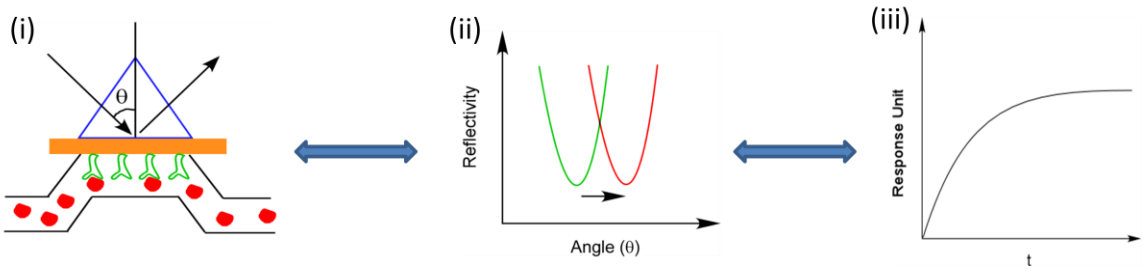

Figure 3-3: (i) Schematic of a Krestchmann configuration SPR, as present in the Biacore system; (ii) reflectivity SPR curves before and after binding; (iii) schematic of a kinetic trace obtained using a Biacore-SPR system.

Figure 3-3i shows a typical Biacore-SPR experiment, where a target protein, immobilized on the metal surface, selectively binds a complementary biomolecule from the solution. This bindings cause the refractive index at the gold-solution interface to change. The change in refractive index lead to a shift in the SPR angle and a change in the reflectivity curve as illustrated in Figure 3-3i. This angle changed, properly converted to RU, is monitored against time as depicted in Figure 3-3iii. This time evolution of the

RU during the surface binding is the kinetic data used to characterize the biological interaction.

3.4 Experimental Procedures

3.4.1 HE4 Antibodies and Antigen

The HE4 antibodies and antigens were provided by Dr. Xiaobo Duan from the BCCA-Vancouver Island Centre. The HE4 antigen was collected from the blood of cancer patients. The HE4 antibodies were monoclonal and produced by hosting in mice. The original HE4 antigen concentration provided was 0.890 mg/mL; and the original concentrations of the HE4 antibodies were 0.840 mg/mL. The original antibody and antigen solutions were diluted using PBS buffer to the desired concentration required in a particular experiment. The antibodies and antigen solutions were stored at -20^{o}C before used.

3.4.2 Procedure for the ELISA Assays

The ELISA sandwich assay, described in section 3.2.1, was used in our experiments. The HE4 antibodies used were numbered as HE4.172 and HE4.B152 and the HE4 antigen used was numbered as HE4.31. These were the serial number given by the BCCA, which can be used to discriminate between different batches of antibodies or antigens. The presence of a “B” indicates that the antibody or antigen is biotinylated. The ELISA experiment was performed on a 96 well ELISA plate (Nunc Maxisorp plate), as shown in Figure 4-1. The plate was first coated with 5μg/mL of HE4.172 antibody (first

antibody) in carbonate buffer (pH 9.5) at 4^{o}C in order to activate the plate. The plate was then washed with washing buffer - phosphate buffered solution (PBS) in a plate washer after the activation. Tris buffered saline + 0.1% Tween 20 (TBST; 200µL per well) was used to block the plates for 2 hours at room temperature. The plate was washed again with washing buffer after the blocking step. Different concentrations of HE4.31 antigen solution which is ranged from 0 to 100 ng/mL (0, 0.00610, 0.0122, 0.0244, 0.0488, 0.0977, 0.0195, 0.0391, 0.0781, 1.56, 3.13, 6.25, 12.5, 25.0, 50.0, 100 ng/mL prepared by a serial dilution) were added to each well (100µl per well) for 1 hour at room temperature. The plates were washed with washing buffer after this incubation period. The secondary antibody, which was biotinylated (HE4.B152) in TBST, was added to each well for 1 hour and the plate was washed. After washing, Streptavidin-alkaline phosphatase (Srep-AP; 100µl per well) was added for 1 hour at room temperature. The plate was washed again. Substrate for alkaline phosphatase (0.2mM CSPD + 5% Emerald II; 100µL per well) was added to incubate each well for ~25 minutes. The plates were read with plate reader.

3.4.3 Procedure for the Biacore Assays

3.4.3.1 Chemicals and Equipments

The Biacore machine used was the Biacore X100 and the sensor chip (gold coated slide modified with a functionalized dextran layer) was the CM5. The binding conditions were established by using the anti-mouse IgG kit (Biacore). The kit includes anti-mouse IgG antibody (1 mg/mL in 0.15 M NaCl), immobilization buffer (10 mM sodium acetate pH 5.0), and regeneration solution (10 mM Glycine-HCl pH 1.7).

3.4.3.2 Procedure

The sensor chip was first premodified with the anti-mouse antibody in order to bind the HE4 antibody (HE4.172) which is produced in mice, as we described before (section 3.1). The anti-mouse antibody binds most of the antibodies types that are produced by hosting in mice. The HE4 antibody and antigen were diluted in PBS to desired concentration before running the experiment. The HE4 antibody (HE4.172) concentration was 25μg/mL and the HE4 antigen (HE4.31) concentration ranged from 0 to 5μg/mL (0, 0.5, 0.625, 0.75, 1, 1.25, 2.5, 5 μg/mL). The first solution run was the HE4 antibody (HE4.172) for 180 seconds at 30μL/min. After the HE4 antibody was immobilized on the sensing chip, an antigen solution (HE4.31 – HE4 antigen) was flown for 80 seconds and washed for 300 seconds at 15μL/min. Finally, the sensor chip was regenerated for 90s (2 times) with glycerine-HCl (pH=1.7) to remove all HE4 antibodies. After regeneration, the process started again using the next concentration of HE4 antigen.

3.5 Results

3.5.1 ELISA Results

The ELISA calibration data is shown in Figure 3-4. It is clear from Figure 3-4 that the fluorescence intensity increased as the concentration of antigen increased. The system was observed to be approaching saturation when HE4.31 antigen reached 60ng/mL.

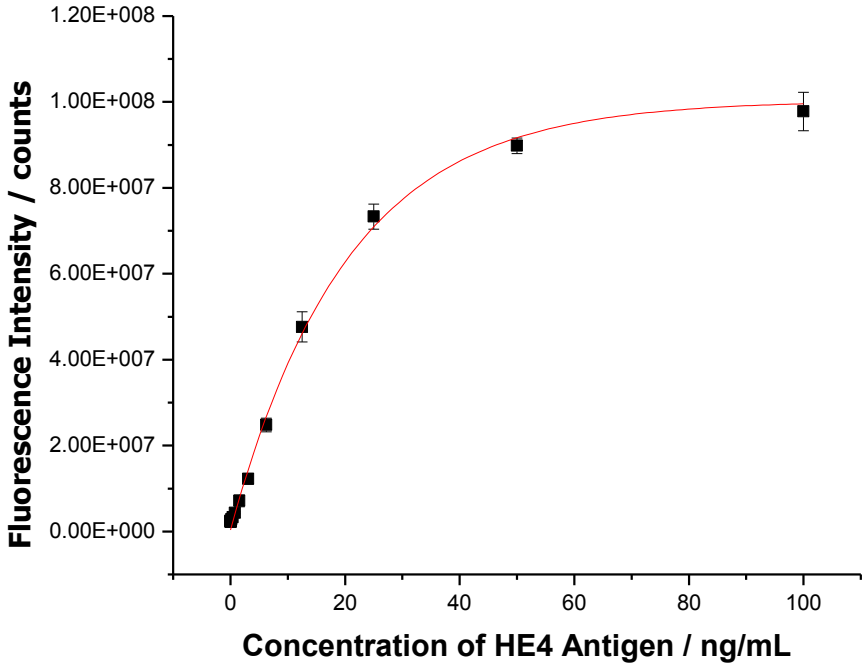

Figure 3-4: Calibration curve of HE4 antigen for the ELISA experiment.

The main results from the ELISA experiments are summarized in Table 3-1. The lower detection limit (LD) was estimated as approximately 0.50 ng/mL (2x background signal) or 0.75 ng/mL (3x background signal). The lower detection limit was calculated by subtract the minimum distinguishable analytical signal (S_m) (equation 3-1) to the average of the background signal and then divided by the slope of the dynamic range as shown in the equation 3-2[57].

$$S_m = \bar{S}_b + ks_b \quad (3\text{-}1)$$

$$LD = \frac{S_m - \bar{S}_b}{m} \quad (3\text{-}2)$$

Where $\bar{S}_b$ represent the average blank signal; k represents an integer number times standard deviation (2 or 3 in our case). s_b represents the standard deviation of the blank signal and m represent the slope of the dynamic range. The dynamic range is the region on the beginning of the graph where it shows linear response[57].

Based on the experiment procedure and the data obtained, there were 2 antibodies required for the ELISA experiments: the capture and the detection (conjugated to an enzyme) antibodies. The total time to perform a single ELISA experiment was roughly one day. However, a great deal time and preparation were required. These extra preparations included plate activation, solution preparation, solution pipetting, plate washing, and plate reading. Also, ELISA plates are designed for single usage. In general, more solution volume is needed for the ELISA technique compared to the Biacore or the nanohole technique, which will be shown in section 3.5.2 and Chapter 4, respectively.

Table 3-1: Short summary of ELISA experiment with HE4 biomarker.

ELISA	**Results**
Detection limit	~0.50 ng/mL to 0.75 ng/mL
Antibodies needed	2
Experiment duration	1 day
ELISA plates	Single usage
Human works required	Lots of pipetting, washing, and solution preparation

3.5.2 Biacore Results

3.5.2.1 Kinetic Graph

A typical kinetic graph (also called sensorgram) outputted from a Biacore instrument is shown in Figure 3-5. The concentrations of the antibody and antigen used for this particular Figure were 25 µg/mL and 2.5 µg/mL, respectively. The other conditions are as described as shown in section 3.4.3.2.

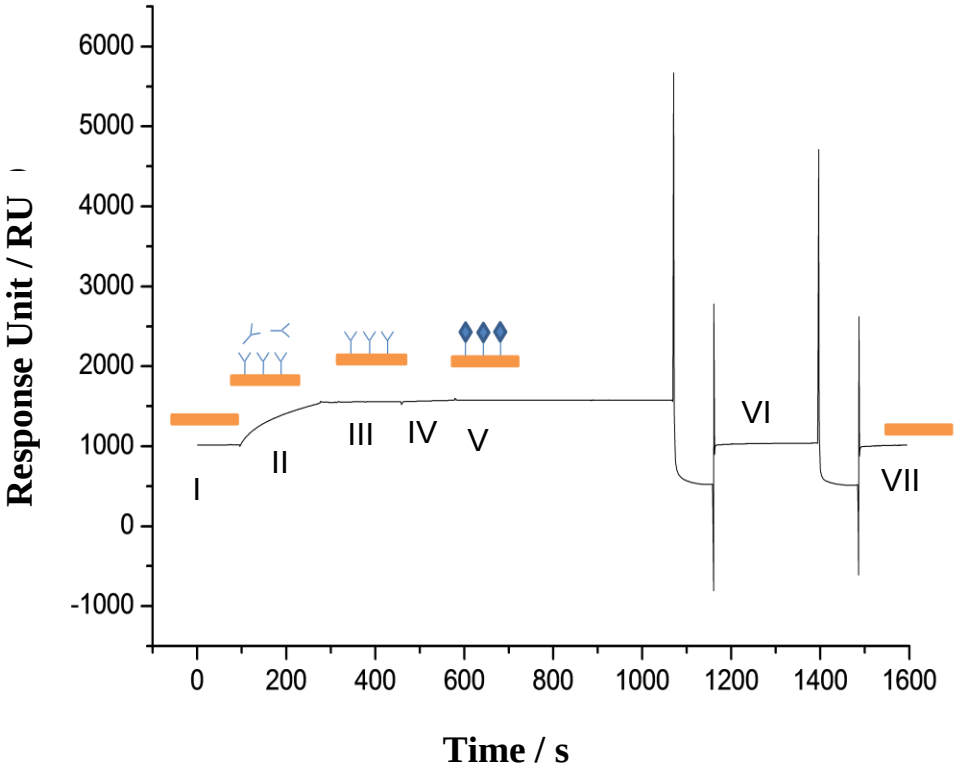

Figure 3-5: Sensogram for the HE4 (2.5 µg/mL) affinity test from a SPR experiment using the Biacore system.

In region I of Figure 3-5, the buffer was introduced to establish a baseline. The antibody solution (25 µg/mL) was flown in region II, leading to an increase in the RU

values against time. After the antibody signal stabilises, buffer solution was introduced in region III to wash away unbound antibody. In region IV, the antigen solution (2.5 µg/mL) was introduced and the RU value increased slightly due to the antigen – antibody binding. This increase is not clear in Figure 3-5; therefore, the region IV section was magnified and it is presented in Figure 3-6 for different concentrations of HE4 antigen. In region V, buffer solution was introduced again to wash away unbound antigen. Region VI in Figure 3-5 contains two regeneration steps performed to wash away both the antibody and antigen. It can be seen that the RU value dropped back to the original baseline before the introduction of the antibody in region VII, indicating that the chip was back to its original condition, and ready for the next cycle.

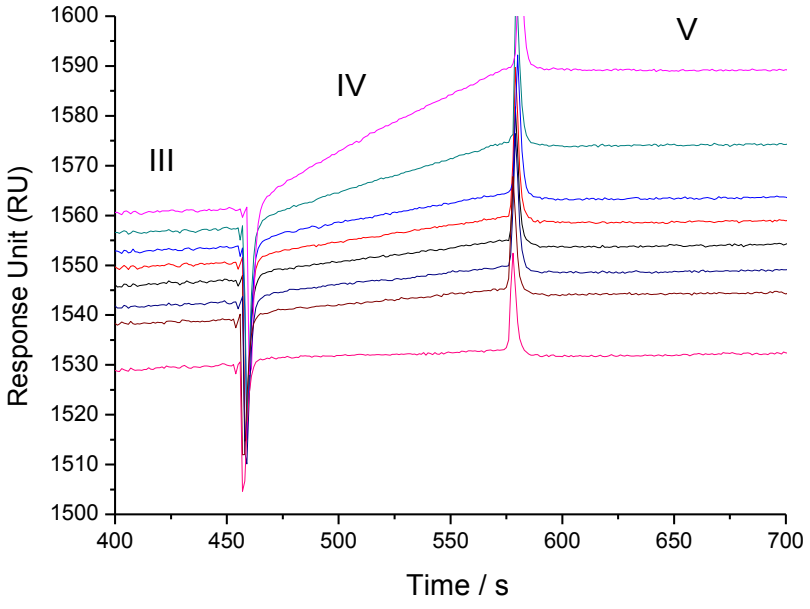

Figure 3-6: Zoom-in antigen binding region (regions III to V in Figure 3-5) for Biacore.

The antigen binding kinetics is shown in Figure 3-6. The RU changed in different values for the different concentrations of HE4 antigen with certain period of time. The different between III and V in Figure 3-6 leading to a calibration curve (Figure 3-7) for the antigen concentration.

The final signal levels of HE4 antigen for each concentration were obtained from Figure 3-6 and they are plotted as a calibration curve in Figure 3-7. In Figure 3-7, the relative response increased as the antigen concentration increased. The lower detection limit was obtained by estimate the (2x or 3x of) background signal. The calibration curve also showed a linear relationship between the HE4 antigen and the relative response. The lower detection limit was determined to be approximately 0.13 μg/mL to 0.20 μg/mL.

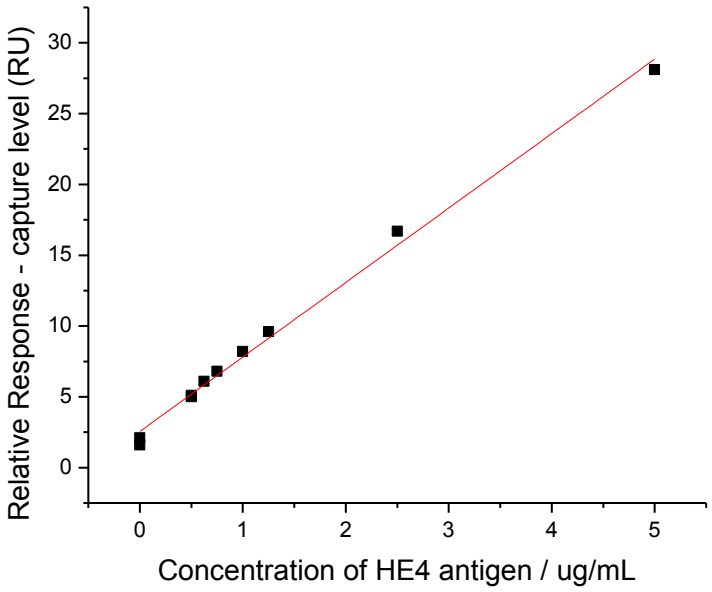

Figure 3-7: HE4 antigen calibration line for Biacore.

The results from the Biacore measurements are summarized in the Table 3-2. We concluded that the lower detection limit was approximately 0.13 μg/mL (2x background signal) to 0.20 μg/mL (3x background signal). There was only 1 antibody needed in addition to those on the premodified CM5 chip. The HE4 antibody (HE4.172) was used to capture the target HE4 antigen (HE4.31). The signal was given by SPR angle change. Again, the total experimental time was around 1 day. However, the actual human work needed was only solution preparation. After solution preparation, the rest of the procedure is automated in the Biacore machine. The sensor chips for Biacore are designed for multiple usages, but the machine requires regular maintenance. The maintenances include weekly desorb (~25 mins) and monthly desorb, sanitize, system check, and inspection on sample area and pump (~60 mins). In most of the steps, you just need to prepare the solutions and take advantage of the automated Biacore system

Table 3-2: Short summary of Biacore experiment with HE4 biomarker.

Biacore	**Results**
Detection limit	~0.13 μg/mL to 0.20 μg/mL
Antibody needed	1
Time needed	1 day
Gold chips	Multiple usage
Solution needed	Relatively smaller (than ELISA)
Human works required	Preparing solution and regularly machine maintenance
Used in BCCA	Narrowing down the choice on the best antibody/antigen pair (save time from few weeks/months to 2-3 days)

Chapter Four: Nanohole Array and Microfluidic Integration

4.1 Nanohole Array

4.1.1 Nanohole Fabrication

The nanohole arrays were fabricated by FEI DualBeam Strata 235 Field-Emission scanning electron microscope with focused ion beam (FIB). The FIB was used to mill[14] the nanohole arrays on a commercial 100 nm gold film deposited on a glass slide (Evaporated Metal Films). A 5 nm Cr layer was used to improve the adhesion between the gold and the glass. The arrays were imaged in the same chamber using a scanning electron microscope (SEM). The energy for gallium ion beam was set to 30keV. The desired pattern of the nanohole can be designed by software. The shape, periodicity, and size of the nanopattern can then be fabricated using the FIB with a resolution of about 10 nm[14]. All samples were fabricated by Mohammad Rahman, a visiting scientist from the Brolo group, using the equipment from the 4DLabs at Simon Fraser University.

4.1.2 Array Design

In order to reach our thesis goal, two types of samples were designed and fabricated. The first one (sample 1) contained four arrays of nanoholes with different periodicities, varying from 400 nm to 550 nm on one gold slide. Periodicity is defined as the distance between nanohole centers. Each nanohole was 200 nm in diameter. This sample allowed us to test the surface plasmon response for different periodicities to choose the best design for the next part of the experiment. Based on the results from

sample 1, twenty-eight (7x4) nanoarrays were fabricated on the same slide, arraged as show in Figure 4-1 (sample 2). The distribution of the arryas in sample 2 was chosen in order to allow a direct comparison to the data obtained from the ELISA and the Biacore-SPR assays. The footprint of each array was 15 µm x 15 µm and the distance between each array was 150 µm and 60 µm from side to side. Each nanohole was 200nm in diameter and the periodicity was 420nm. Multiple rows enable the recording of multiple binding experiments at the same time. Each for these experiments might have different concentrations implemented by the solutions run through the columns.

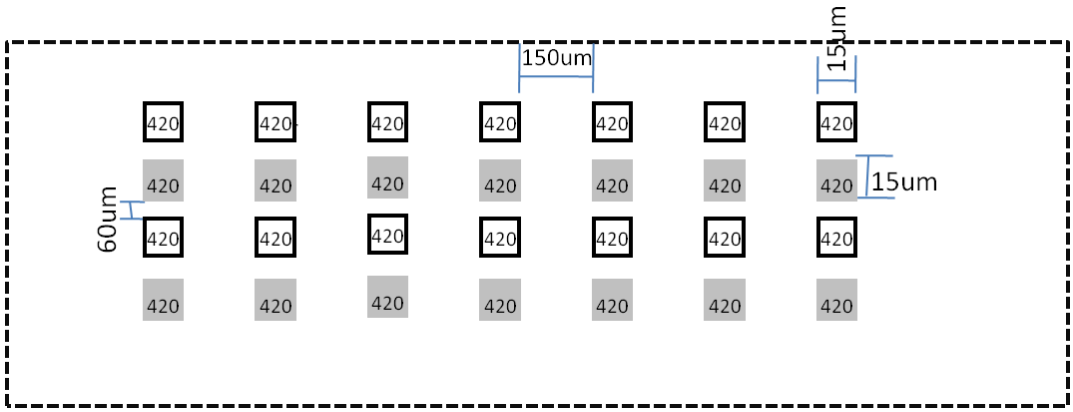

Figure 4-1: Design of the sample 2, containing 28 nanohole arrays. The periodicity, the array footprint and the distance between the arrays are indicated in the Figure.

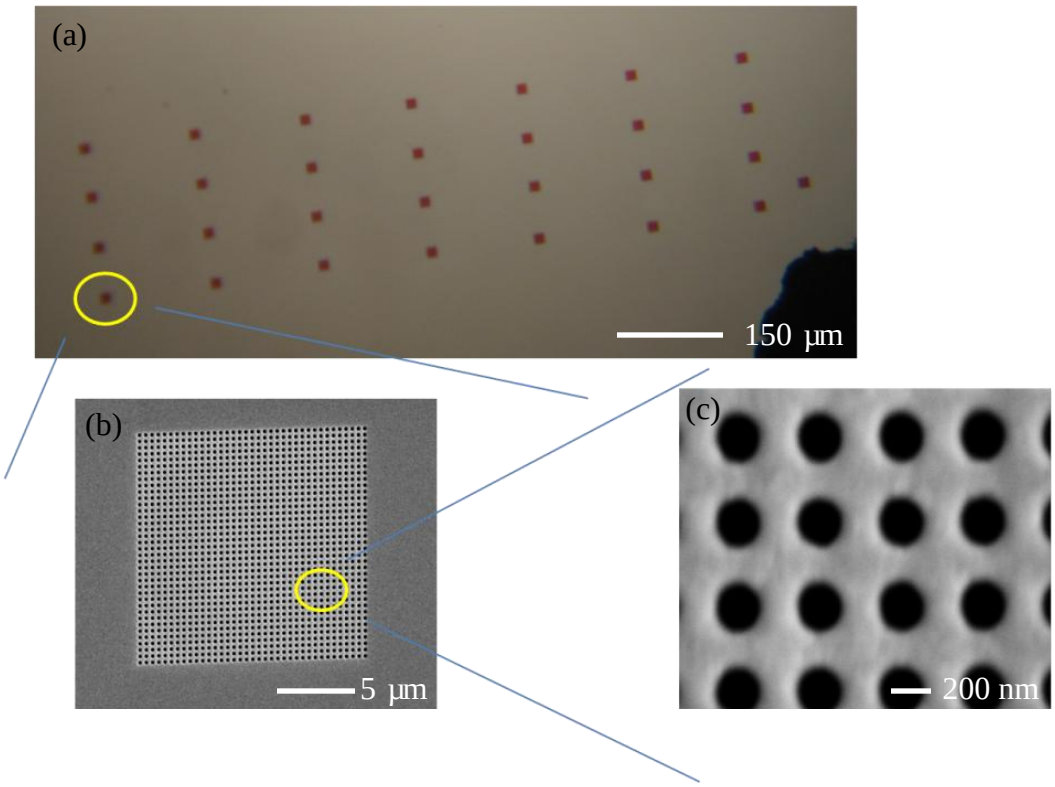

Figure 4-2: Image of Sample 2 under the optical microscope (a). SEM image of a single nanohole array image (b). SEM image of a nanohole array at higher magnification (c).

4.2 PDMS Micro Fluidic Channel

The nanohole arrays are just the sensing elements. A system to deliver solution to the sensor surface, for surface modification and analysis, need also be included. This solution delivery system is based on microfluidic chip[58]. The microfluidic channels allow the flow of protein solutions to the gold slide. In our experiment, the channels were made using polydimethylsiloxane (PDMS)[58]. Since the PDMS chip is single use only, a silicon master was designed and fabricated first[58]. This master was the template from which identical patterns of PDMS chips were produced easily.

4.2.1 Silicon Master

The master for the production of the PDMS chips was fabricated by photolithography on a silicon wafer[58]. The schematic diagram for this process is shown in Figure 4-3. Figure 4-3a represents a silicon wafer. In Figure 4-3b, a negative photoresist (SU-8 50, 2 mL) was added to a silicon wafer, and was then spin coated to make a smooth layer with maximum spin rate of 1800 rpm (increase rate 100 rpm/s) for 30 seconds. The wafer coated with photoresist is then bake at 65^{o}C for 6 to 10 minutes and then bake at 95^{o}C for 30 minutes. After baking, a mask with a microfluidics pattern was placed on top of the wafer coated with the photoresit, and the wafer was then exposed to UV light (~350 to 400 nm) as shown in Figure 4-3c for 60 to 100 seconds. In the exposure stage, only the photoresist which is covered by the mask will be remain on the waver. After exposure, the wafer was baked at 65^{o}C for 1 minute and at 95^{o}C for 5 to 10 minutes and developed with SU-8 developer while constant stirred for 10 minutes. Finally, the wafer (silicon master) as shown in Figure 4-3d was ready to produce PDMS microfludic channel chips (chapter 4.2.2).

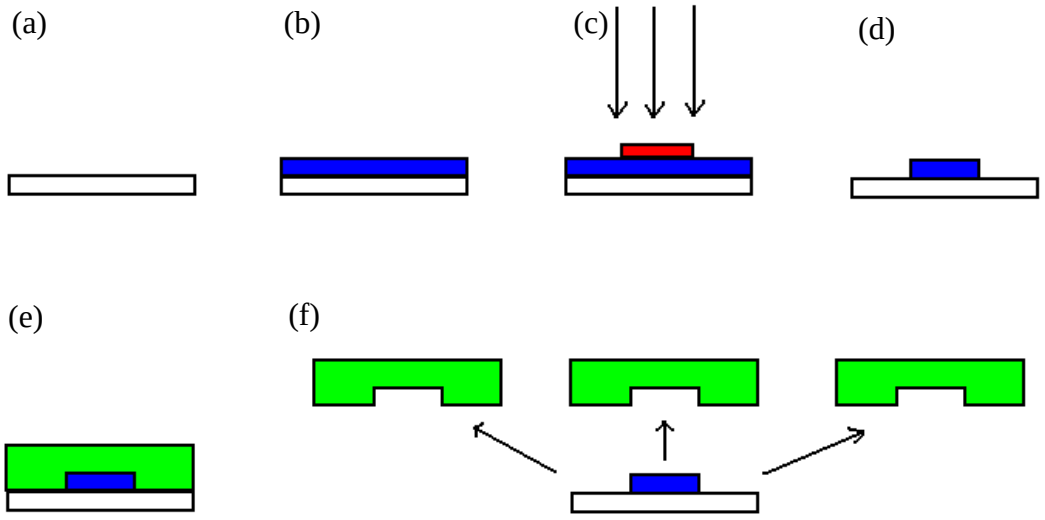

Figure 4-3: Schematic diagram on making PDMS master and PDMS making. (a) A silicon wafer (b) coated with photoresist. (c) A mask is placed on wafer and exposed to UV. (d) The mask is developed and ready to use. (e) PDMS gel is placed on the silicon master. (f) After baking, the PDMS microfludic channel is ready to use and the master can be used for making the next microfludic channel.

4.2.2 PDMS Chips

The PDMS chips, containing the microfluidic channels, were made by mixing Sylgard 184 silicone elastomer base and silicone elastomer (Dow Corning) curing agent using a ratio of 12:1 by weight. The silicone elastomer gel (~24 g) was mixed with curing agent (~2 g). The mixture was degassed under vacuum (~20 minutes) in order to get rid of all gas bubbles. After the degassing, the mixture was poured on the master and the system was degassed again. After this, the master with a layer of PDMS on top as shown in Figure 4-3e was placed into an oven (~80^{o}C) for 25 minutes. After baking, the PDMS was peeled out from the master and the master can be used for making next microfludic

channel. Based on the design of channel, holes will be punched on the appropriate places (inlet and outlet as describe in section 4.2.3) with hole puncher (sensipress+, NWSL).

4.2.3 Dilution Chip

In order to produce a calibration curve and cut down the experiment running time, a dilution chip pattern (Figure 4-4) was designed[59]. The basic goal of the dilution chip is to provide a concentration gradient across the nanohole array sensing elements. The chip combines two streams, containing different concentrations of the analyte of interest and allowed them to flow for certain distance in order to be mixed properly. The concentration of the output can be controlled by controlling the ratio of the concentrations of the input solutions. Multiple concentrations can be generate from two initial inlet by multiple steps dilutions[60].

The dilution chip in Figure 4-4, present three inlet channels (i, ii, iii) and one outlet channel (iv). Inlet channels (i) and (ii) were used to generate a series of solutions of the desired protein with different concentration downstream to provide a calibration curve. One of the inlets (i) was filled with the buffer (PBS). The two solutions introduced in the inlets streamed through the channels and mixed in the first mixing region. The outputs from the first mixing regions are three solutions. One of them has the same concentration as the initial solution in the inlet (i), the other is the pure PBS introduced in inlet (ii), but the solution between them will be a perfect mixture, with 50% of the initial concentration in inlet (i). The three concentrations resulted from first region is now flowing into second mix region which is containing now four “zig-zag” paths. These

mixing processes are then repeated four times. At the end of the channels, after all mixing stages, six different concentrations of antigen will result across the area indicated as "nanohole" in the Figure 4-4, with concentration raging from 0 to 100% of the initial concentration of the protein. The transmission across those channels allow the generation of a calibration plot. The remaining inlet channel (iii) was used to flow a sample with unknown concentration. The results from the unknown sample were fit within the calibration curve provided by the other channels. The outlet (iv) was used to collect the waste solution.

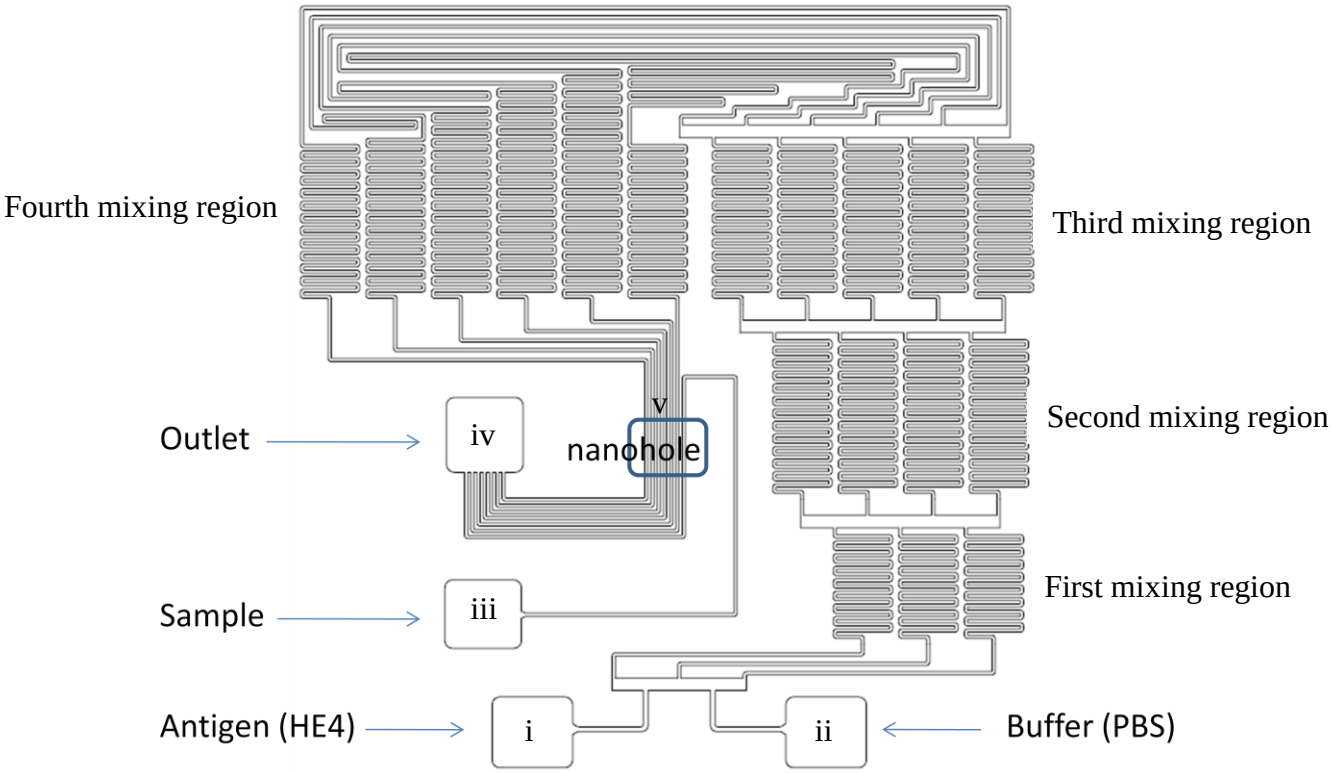

Figure 4-4: Microfludic pattern of the dilution chip. The channel width and height is around 90 μm.

4.2.4 Array Alignment

The array and of nanoholes (sample 2, shown in Figure 4-1 and Figure 4-2) and dilution chip channels were aligned manually using an optical microscope. The actual image under the microscope for position (v) in Figure 4-4 is shown in Figure 4-5. The most left channel in Figure 4-5, was used to flow the unknown sample and the other channels were used for calibration with the different known concentrations of antigen produced by the dilution chip.

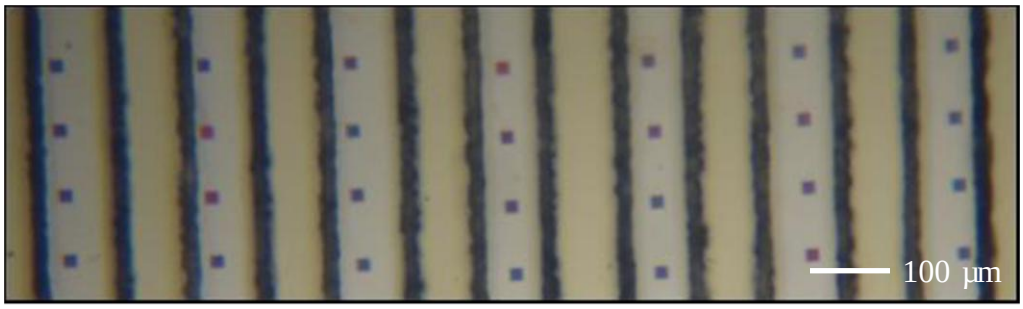

Figure 4-5: Optical image of Sample 2 aligned with the dilution chip under the microscope.

4.3 White Light Transmission through the Nanohole arrays

4.3.1 Experiment Setup

The transmission experiment setup is shown in Figure 4-6. A 100 watt halogen bulb was used as the white light source. An optical microscope (OLYMPUS BHT) was used to focus the light on the gold sample. The light that passed through the nanohole

arrays was then collected by an optical fibre and measured with a handheld spectrometer and the resulting transmission spectrum was displayed on the computer by the data acquisition software (Ocean Optics – OOIBase 32 Platinum). The sensor setup consisted of 3 layers. The very bottom layer was a glass slide with a gold layer where the nanoarray pattern was located. The middle layer was the microfludics (made by PDMS) layer where solution would be allowed to flow. The top layer was a plastic chip which was used to stabilize the other two layers on the sample holder with screws, and distribute the pressure evenly across the PDMS chip. The actual assembled sample is shown in the Figure 4-6 together with a schematic representation of the experimental setup.

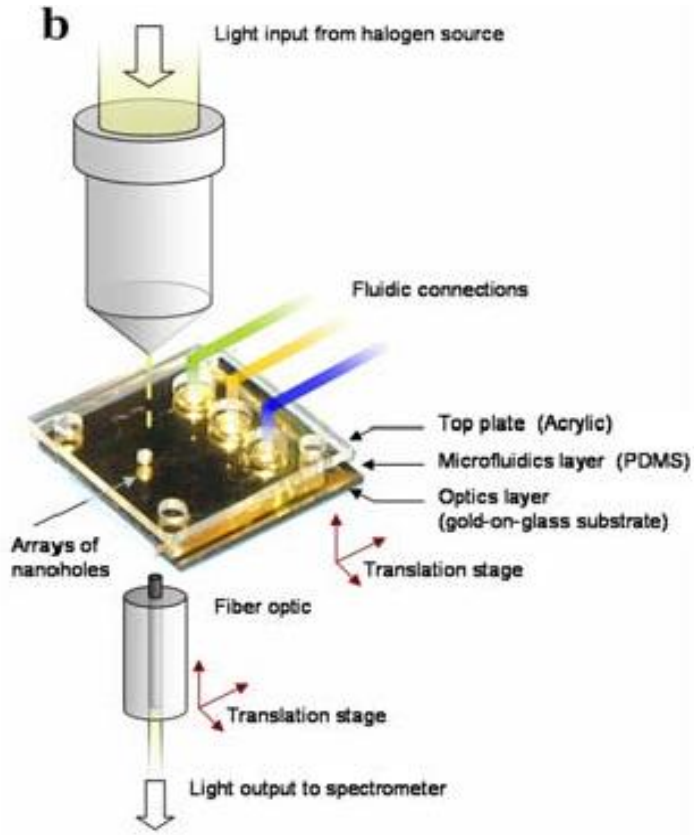

Figure 4-6: Schemaic representation of the setup for transmission measurements through nanohole arrays. "With kind permission from Springer Science+Business Media: <Microfluids and Nanofluids, Nanohole arrays in metal films as optofluidic elements: progress and potential, 4, 2008, 107, Sinton, D., Gordon, R., Brolo, A., figure 4(b)>."

4.4 Imaging SPR using nanohole arrays

The affinity tests were also conducted using a charge-coupled device (CCD) image setup. In that case, the changes in intensities of a monochromatic light transmitted through each array were followed[61]. The white light transmission spectra indicated that the SPR peak shifts to higher wavelength when the refractive index at the gold dielectric interface increases[12] as stated in section 2.2.1. This will be further tested and explained in the section 4.6.1.3. Therefore, if the wavelength of the incident light is fixed and the SPR

peak shifts due to a molecular adsorption, one would observe a change in the intensity of the transmitted light at that particular wavelength. This process is illustrated in Figure 4-7. When the wavelength of incident light is fixed on the left side of the transmission peak, the intensity will decrease as the peak shifts to the red end of the spectrum. However, if the wavelength of incident light was fixed on the right side of the transmission peak, the intensity will increase as the peak shifts to the right. The advantage in this setup is that multiple arrays can be monitored at the same time on one sample in one experiment by using a CCD camera to measure the intensity of the transmitted light through all arrays at once. This advantage is particularly important for the dilution chip described in section 4.2.3, since it permits a calibration curve to be obtained in real time for each measurement.

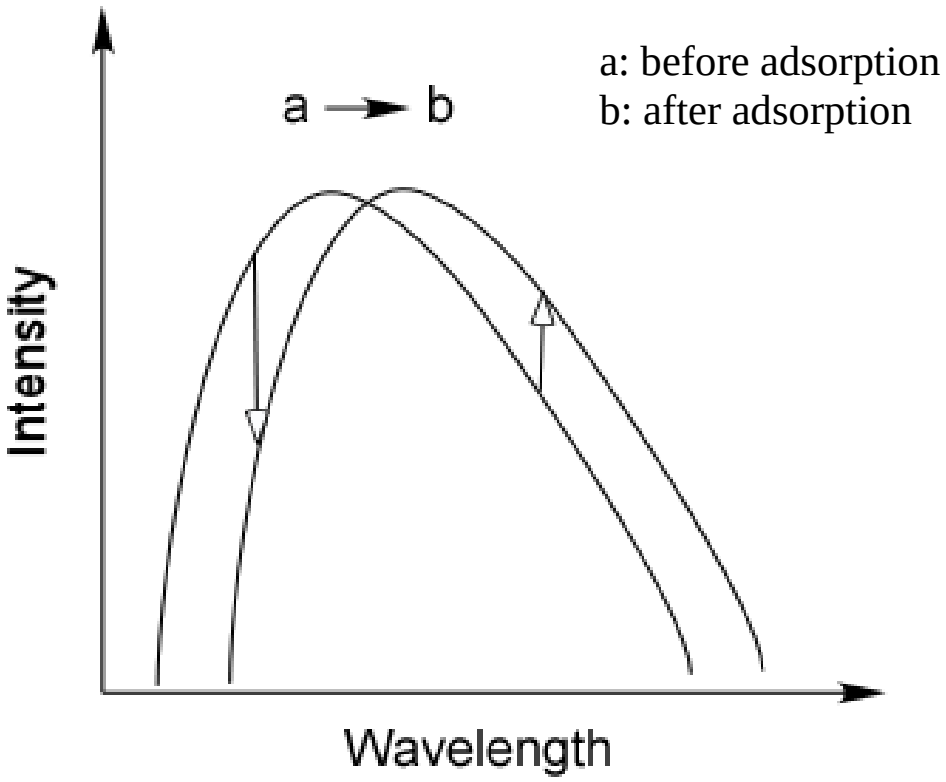

Figure 4-7: Principle of the intensity changes observed with the imaging SPR setup. The intensity of a monochromatic source decreased after adsorption when the wavelength is fixed on the blue side of SPR peak. The decrease occurs because the SPR peak shifts to the red. On the other hand, the intensity increases after adsorption when the wavelength is fixed on the red side of the SPR peak.

4.4.1 Imaging SPR Experimental Setup

A scheme of the experimental setup for imaging SPR through arrays of nanoholes is shown in Figure 4-8. A red coloured LED ($\lambda = 663 \pm 12$ nm with 50% maximum peak height) was used as the light source. The light beam passed through two objective lenses (20x) before reaching the sensor. The objective lenses allowed us to adjust the position and size of the light beam. The light then passed through the gold (with nanohole array integrated with microfluidics) sample and the transmitted light was collected by a CCD

camera (CoolSNAP HQ^2, photometrics). A multichannel syringe pump (New Era Pump Systems, NE-1800) was connected to the PDMS chip on the gold sample in order to control the flow rate of the solutions. The images were acquired by commercial image software (Voodoo 1.2, photometrics) The scheme of CCD image setup and an actual image of a Sample 2, with 28 arrays, is shown in Figure 4-8.

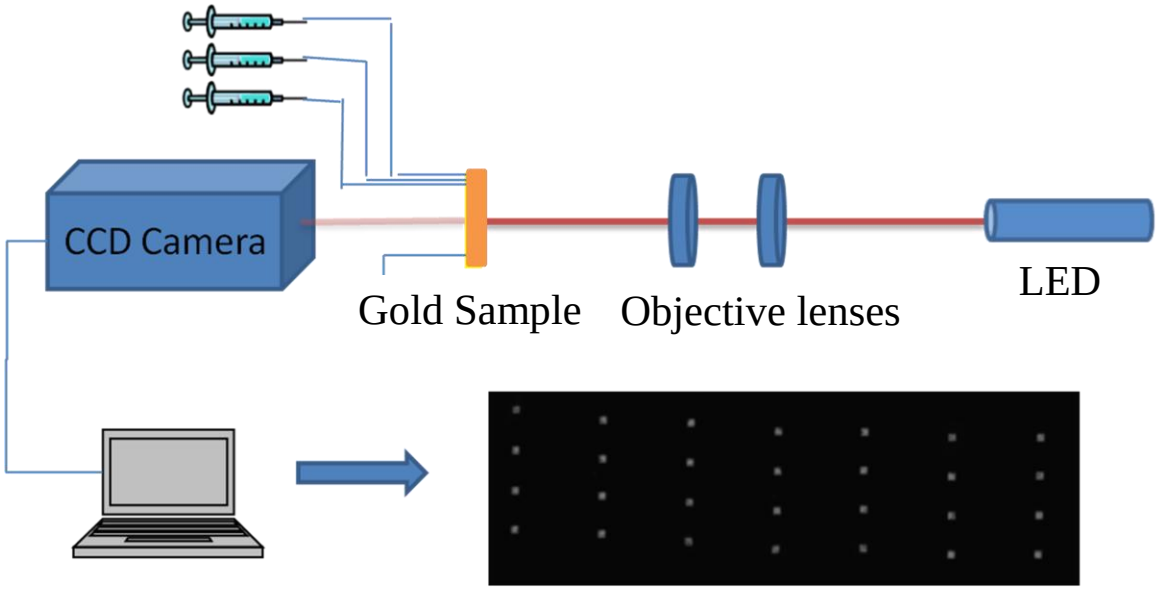

Figure 4-8: Schematic diagram of CCD setup and the nanohole array image displayed.

4.5 Experimental Procedure

4.5.1 White Light Transmission

The sample 1 (described in section 4.1.2) was initially used for the white light transmission measurements. The sample was integrated in a microfludic chip and placed into the transmission setup shown in Figure 4-6. After that, a lower magnification (10X) microscope lens was used to find the arrays. A higher magnification (50X) lens was used

to narrow the light beam on individual nanohole arrays. The transmission spectra were then collected by the optical fibre coupled spectrometer and recorded using the Ocean Optics program (section 4.3.1).

4.5.1.1 Transmission Spectra for Arrays of Different Periodicities

The spectra of the arrays of nanoholes with different periodicities (sample 1, described in section 4.1.2) experiments were done using the white light transmission setup. Sample 1 contained 4 arrays (with 4 different periodicities). The transmission spectra of each were collected under the same conditions of illumination (light source and power). First the transmission spectra for each periodicity were taken from the gold-air interface (bare nanohole gold layer without the PDMS chip, the acrylic layer or any solution on top).

After that, Sample 1 was integrated in a simple microfluidics structure containing a straight channel in PDMS. Glucose (Sigma-Aldrich) solutions of different concentrations were prepared and flown over the nanohole arrays. A spectrum was collected for each array at each glucose concentration. This experiment allowed the determination of the sensitivity of the arrays to changes in bulk refractive index.

4.5.2 Imaging SPR

Sample 2 (section 4.1.2) was used for all imaging SPR measurements. The sample was integrated to the microfluidic dilution chip (section 4.2.3) and mounted in a

horizontal position as described previously in Figure 4-8. The LED light was turned on for at least 40 minutes before use in order to reach intensity stabilization. An example of an actual image is shown in Figure 4-8.

4.5.2.1 Calibration using Glucose Solutions

Glucose solutions of different concentrations were used to calibrate the response of Sample 2 in the imaging SPR setup to changes in bulk refractive indexes, using the dilution chip. In this case, both sides of the inlet channels of the dilution chip were filled with the same solution, from pure water to 1.5 M aqueous glucose. The refractive index of each solution, including pure water was measure by a commercial refractometer (pocket refractometer, ATAGO). One image of the entire area of interest of the Sample was taken for each glucose concentration. All 28 arrays (7x4) were then imaged under the same conditions, and the intensity for each array was plotted against the bulk refractive index as calibration.

4.5.2.2 Calibration of the Surface Sensitivity of the Imaging SPR Setup Using the Biotin-Streptavidin System

Biotin and streptavidin are known as one of the best systems as a model for protein binding investigation[62], due to their high affinity constant ($K \sim 10^{15}$)[62]. The calibration was done using Sample 2 integrated with the dilution chip (section 4.2.4). The experimental steps of the calibration process were: 1) The gold sample was modified with cysteamine monolayer by immersed into aqueous cysteamine solution (~6 mM) overnight.

2) After the premodified (with cysteamine) gold sample is rinsed with water and PBS buffer, both inlet channels were filled with PBS buffer and the channels were filled with PBS at a flow rate of 10 μL/min (maximum 20 μL/min) to create even pressure in all the channels; 2) The solution on both inlets were replaced by NHS-biotin (Sigma-Aldrich) solution (25 μg/mL) in DMSO that were introduced through the channels for 45 minutes at 10 μL/min flow rate. A biotin monolayer was allowed to be formed at the gold surface in this step and all arrays in each channel are considered to have experienced "identical" surface modification; 3) The inlets were again filled with PBS buffer to wash away any unbound biotin at 10 μL/min for 40 minutes; 4) streptavidin solution was introduced in one inlet and the other inlet was filled with PBS buffer in order to generate a concentration gradient (0 to 50 μg/mL) across the channel, as discussed in section 4.4.1. Images were taken in each of these steps.

4.5.2.3 HE4 Imaging SPR Experiments

Sample 2 and the "dilution chip" were also used to collect kinetic data for the binding between HE4 and its antibody. The gold sample was premodified with dithiobis(succinimidyl undecanoate) (DSU) (~2 mM) from DOJINDO overnight. The premodified DSU layer is used to bind the primary amine of proteins, since the HE4 antigen is not expected to bind to the gold sample efficiently as shown in Figure 4-9. PBS solution was used first in both inlets, in order to push eventual air bubbles out of all channels and establish a baseline. The surface was then coated with the HE4 antibody, which was introduced through the channels for at least 60 minutes at 10uL/min to ensure that saturation was reached. The HE4 antigen (5 μg/mL) was then introduced in one of

the inlets and PBS on the other to create the concentration gradient. The HE4 antigen solutions were flown for ~90 minutes at 10uL/min after the antibody reached saturation.

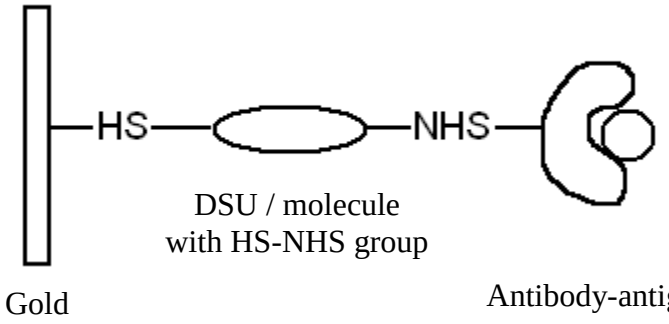

Figure 4-9: Schematic diagram of NHS group binding with protein on gold surface

4.5.3 Sample Cleaning

The sample was cleaned between each usage by sonicating in acetone for 5 minutes (1 times) and in ethanol for 10 minutes (3 times). After the sonication, the sample was placed in the plasma cleaner (Harrick) with high RF level under vacuums for 20 minutes. After that, the transmission spectrum was measured and the sample was checked for cleanness (if the EOT peak was back to the original wavelength). The sample was also checked once every month by Fourier transform infrared spectroscopy (FTIR) in order to make sure the cleanness of sample surface.

4.6 Results

4.6.1 White Light Transmission Spectra

4.6.1.1 Effect of the periodicity

The wavelength of maximum of transmission through arrays of nanoholes on gold film is expected to depend on the periodicity of the array[61]. The transmission spectra from the arrays on Sample 1, described in section 4.5.1.1, are shown in Figure 4-10. Each spectrum was normalized by its highest intensity. All spectra were plotted in the same graph in Figure 4-10 in order to compare the effect of the periodicity on the wavelength of the maximum transmitted light. The wavelength value of the SPR peak was observed to red-shift when the periodicities increased[61], shown below in Figure 4-10, as expected.

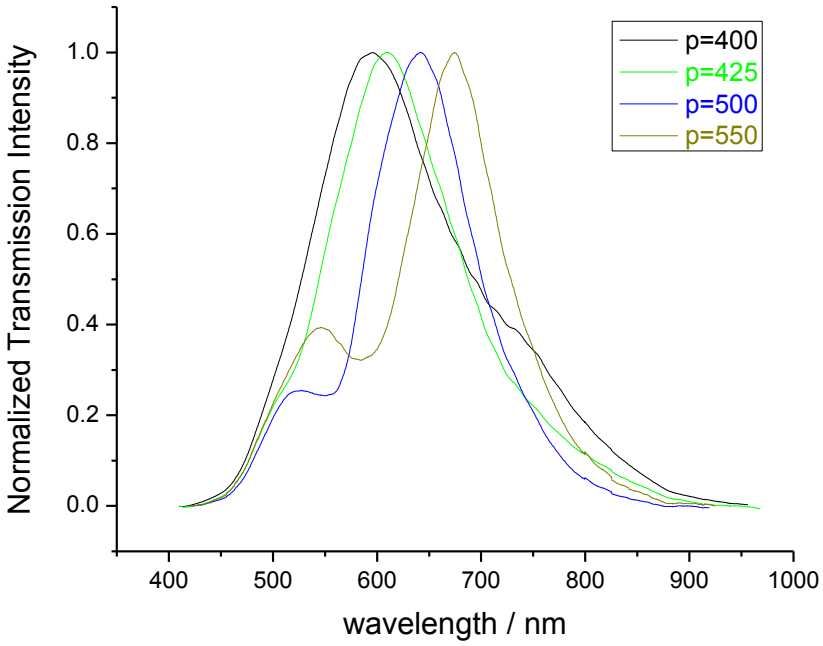

Figure 4-10: Transmission spectra for bare gold under air with different periodicities.

This result can be easily explained by equation 2-5. By increasing the periodicity, the parallel component of the incident light momentum decreased. Therefore, in order to match the k_x and k_{sp}, the wavelength value of SPR peak are expected to increase (red-shift). The following ratio can be obtained from Equation 2-5:

$$k_x = \frac{a}{\Lambda} = k_{sp} = \frac{b}{\lambda} \quad (4\text{-}1)$$

$$\frac{a}{b} = \frac{\Lambda}{\lambda} \quad (4\text{-}2)$$

Where a and b represent constants of the remaining terms in k_x and k_{sp}. From Figure 4-10, the ratio (a/b) can be summarized in Table 4-1.

Table 4-1: The effect of periodicity on the transmitted wavelength and the ratio between them.

Periodicities (nm)	Wavelength (nm)	Ratio (a/b)
400	596	0.67
425	610	0.70
500	642	0.78
550	674	0.82

Based on the equation 4-2, in an ideal situation, this ratio (a/b) should be identical among all arrays. However, the experimental results are different than expected. A possible reason might come from our setup in transmission. In our transmission setup, we used an objective lens to focus the light source which might give us an incident angle slightly greater than zero. Thus, the ratio (a/b) would be changed as well. Although, the ratio did

not match identically to each other, the change in periodicities and wavelength still follow the expected trend.

4.6.1.2 Effect of the Bulk Refractive Indexes

Different concentrations of glucose solutions were used to calibrate the nanohole arrays of various periodicities to their response to bulk refractive index changes from the solution side. Figure 4-11 shows that a red shift was observed when the concentration of glucose (or refractive index of solution) was increased. In this experiment, the periodicity is fixed at 450 nm and the only factor changed is the concentration (refractive index) of the glucose solutions. As we refer back to the equation 2-5, SPR wavelength is expected to shift to greater values when the refractive index (dielectric constant) of solution at the gold interface increases.

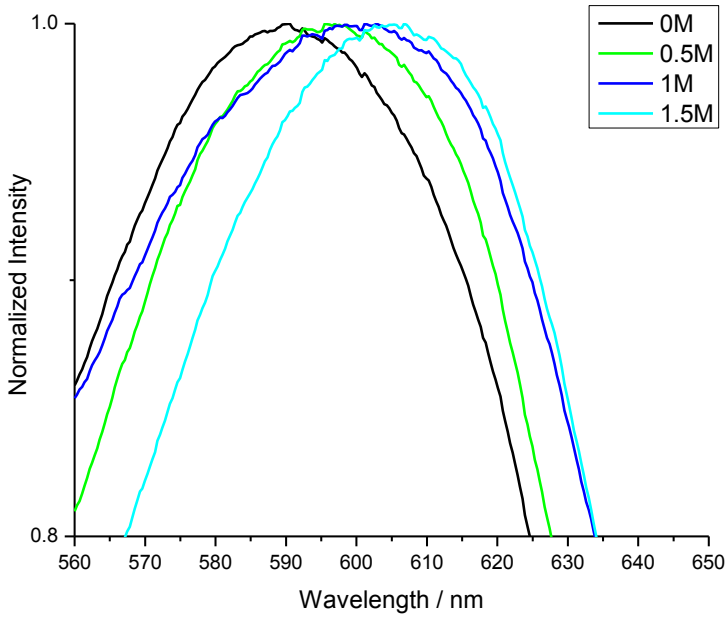

Figure 4-11: Transmission experiments for a nanohole array in contact with different concentration of glucose solutions. The hole diameter is 200 nm and the periodicity is 450 nm.

Based on the Figure 4-11, the Figure 4-12 can be plotted in term of wavelength and refractive index changed. The refractive index of different concentration of glucose solutions were measured with a refractometer and the according wavelength were estimated from the Figure 4-11.

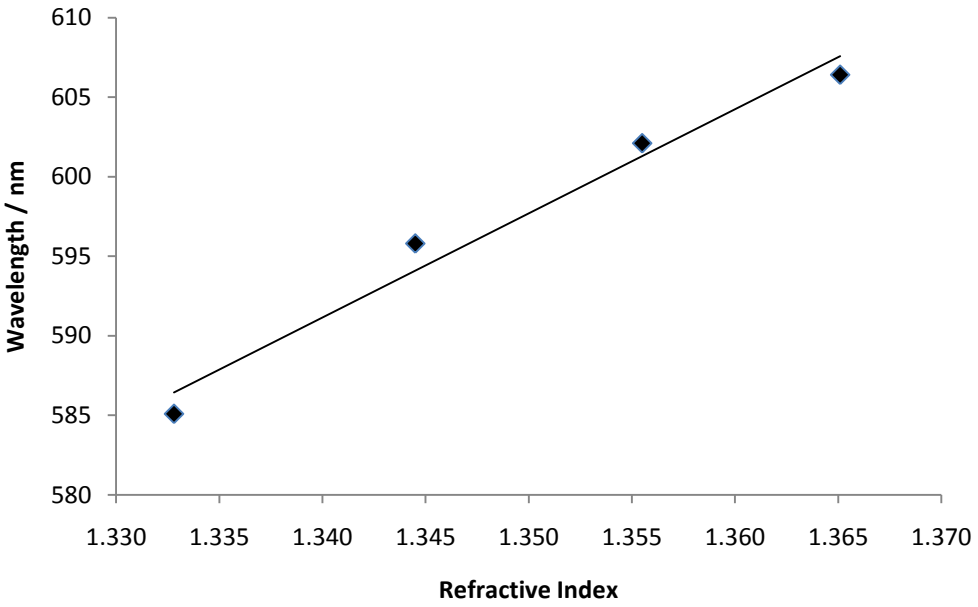

Figure 4-12: The effect of the bulk refractive index on transmission experiment for a nanohole array. The wavelength is estimated based on Figure 4-11.

4.6.1.3 White Light Transmission Summary

The white light transmission measurements show that the SPR wavelength of transmitted light red shifts when the periodicity of the nanohole arrays increased. Although the experiments did not show a perfect match with the predicted regarding the (a/b) ratio, it followed the expected trend. The results indicated that the experimental setup is reasonable and it is working properly. This was further proved by a glucose calibration experiment. In the glucose experiment, the peaks of transmitted light red shifted as the refractive index of the solution increased, as we expected. Although our main focus is not on the evaluation of the white light transmission, the experiments helped us to get a better understanding about your system and to develop good practice to perform the SPR with arrays of nanoholes.

4.6.2 Imaging SPR Results

4.6.2.1 Calibration with Glucose Solutions

The sample 2 was used in the all imaging SPR experiment. This sample was integrated with the dilution chip (section 4.2.4) and used for imaging SPR. The first step, however, was to calibrate the imaging system using different concentrations of glucose solutions. This calibration provided us with information regarding the sensitivity for this system. The intensity differences between the glucose solutions and the pure solvent (water) were calculated for each array. The percent intensity changes were then averaged and plotted against the refractive index of the solutions as shown in Figure 4-13.

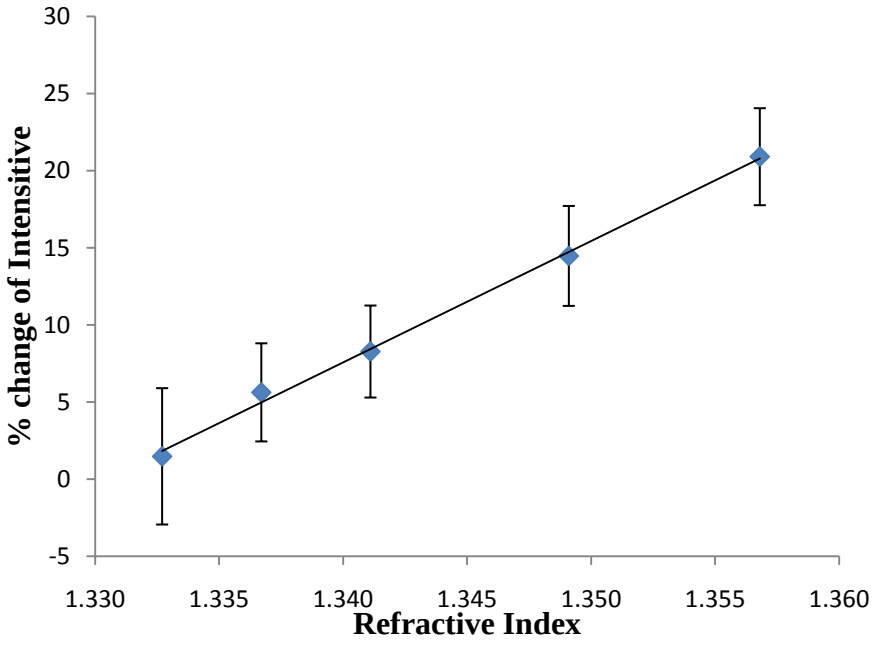

Figure 4-13: Glucose Calibration experiment for Sample 2 integrated with the dilution chip using the imaging SPR setup. The data points are the average of 28 arrays and the error bar are calculated by standard deviation of 28 arrays.

In Figure 4-13, a linear relationship was observed between absolute value of average % intensity change (28 arrays) and the refractive index. The error bars represent the standard deviation of 28 arrays. This relationship could be used to estimate the effect refractive index changed on the gold surface as discussed further in chapter 5. In Figure 4-12, we observed that the variation of response is large (large standard deviation value) but the average responses follow a good trend. This is probably due to the slight array to array variations due to fabrication. Although all parameters of the arrays should be the same, there are defects in some of arrays and small errors due to the instrument. The same error might happen in all experiment; however, if the sample size (number of arrays) are large enough, the error will be very small.

4.6.2.2 Using the Biotin-Streptavidin system to test the sensitivity of our imaging SPR setup to probe protein binding

After calibrating Sample 2 in the imaging system, the next step was to probe the sensitivity of the device in the imaging setup to measure protein binding. As discussed in section 4.5.2.2, the biotin-streptavidin system, a well known affinity pair[62], was used in these tests. The general procedure for all experiments was described in section 4.5.2.2. The final intensities were recorded in PBS solution, to avoid contributions from differences in refractive indexes from streptavidin solutions of different concentrations. The response of the intensity changes (in %) against different concentration of streptavidin is shown in Figure 4-14. The error bar in the graph is the standard deviation of all arrays in the same column.

In the previous section, we have determined the signal response of our system to glucose concentration (bulk refractive index) changes. In this experiment, we are eliminating the contribution from the solution, by measuring the image always in the presence of PBS. Therefore, the only contribution to the refractive index change is due to the protein binding

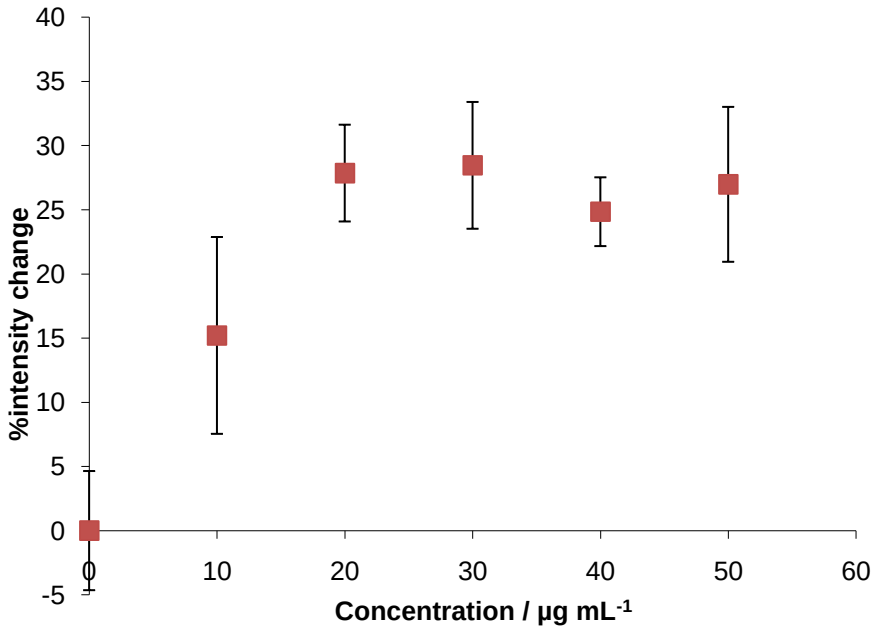

Figure 4-14: Surface binding (biotin-streptavidin) experiment using Sample 2 with the dilution chip in imaging SPR mode. The data points were corrected by the pure PBS channel to 0%. The error bars are the standard deviation of all arrays in the same column.

In Figure 4-14, the %intensity change increased as the concentration of streptavidin increased up to the limit where the streptavidin concentrations reached 20 µg/mL. The flat region in the graph at higher concentration is assigned to surface binding

saturation. Therefore, any concentration above the critical concentration does not increase the amount of adsorbed species at the surface of the nanohole sensors.

4.6.2.3 HE4 Kinetic

The procedure and experimental setup used to investigate the HE4 binding affinity followed the steps in chapter 4.4.3. The images were acquired against time and the intensity changes (always relative to the image at t = 0 s) were then calculated. The integrated intensities of each array at a different time are plotted. Figure 4-15 is one sample graph of antigen concentration equal to 5 μg/mL and the other conditions as described in section 4.5.2.3.

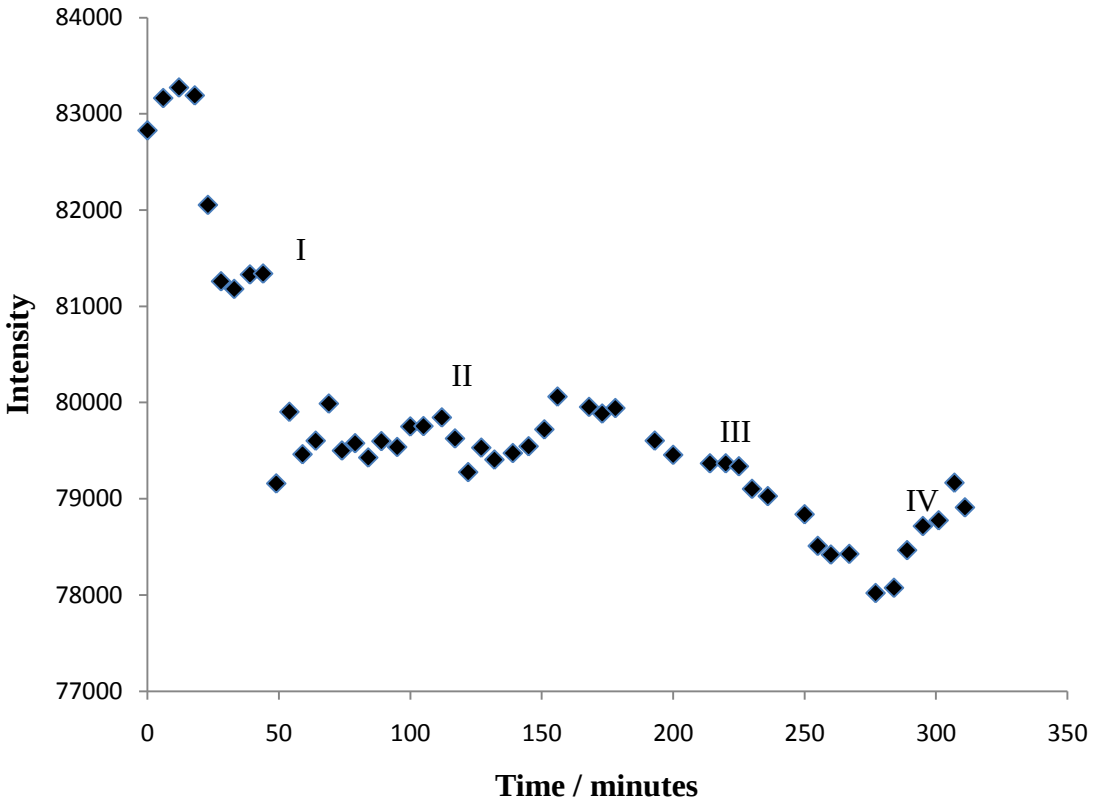

Figure 4-15: Example of one raw kinetic data of the HE4-HE4 antibody adsorption with antigen concentration equal to 5 µg/mL.

As explained in section 4.4, in the kinetics experiments, the wavelength of incident light was fixed to the left side of the transmissions peak. Therefore, in Figure 4-15, we observed that the intensity of arrays decreased as species adsorb to the surface. Region I (0-50min) correspond to the adsorption of the HE4 antibody, which is first immobilized to the surface to provide a target for the HE4 proteins. The antibody immobilization reached saturation, as it can be observed in region II (50-150min). The HE4 protein (antigen) was introduced in region III (150-175min) and the intensity decreased indicating the adsorption of the protein to the immobilized antibody. Finally,

PBS solution was introduced to flush unbounded or weakly bounded species in region IV (175-325 min). This was accompanied by an increase in intensity in region IV.

4.6.2.4 HE4 Calibration

As discussed in section 4.4.1, the dilution chip allows the calibration and the analysis simultaneously on the same chip. Figure 4-16 shows the calibration data in terms of % intensity changes vs concentration of HE4 antigen in μg/mL. The error bars represent the standard deviation among 4 arrays in the same column (see Figure 4-16). The red square in the graph is for a solution introduced in the sample lane (see Figure 4-16). This solution would represent an "unknown" concentration from a real sample. In our case, however, a HE4 solution was prepared with a concentration equal to 2.5 μg/mL. When plotted against the calibration line, the estimate value of solution in the sample channel should have been 3.5 ± 1.2 μg/mL. The concentration of the sample obtained from the calibration curve was larger than the expected concentration (2.5 μg/mL). However, if the error is considered, the sample concentration is fitted into the error range. In this experiment, the error bar is still big in term of the result range and this might be able to improve by increasing the sample size (arrays in the same column).

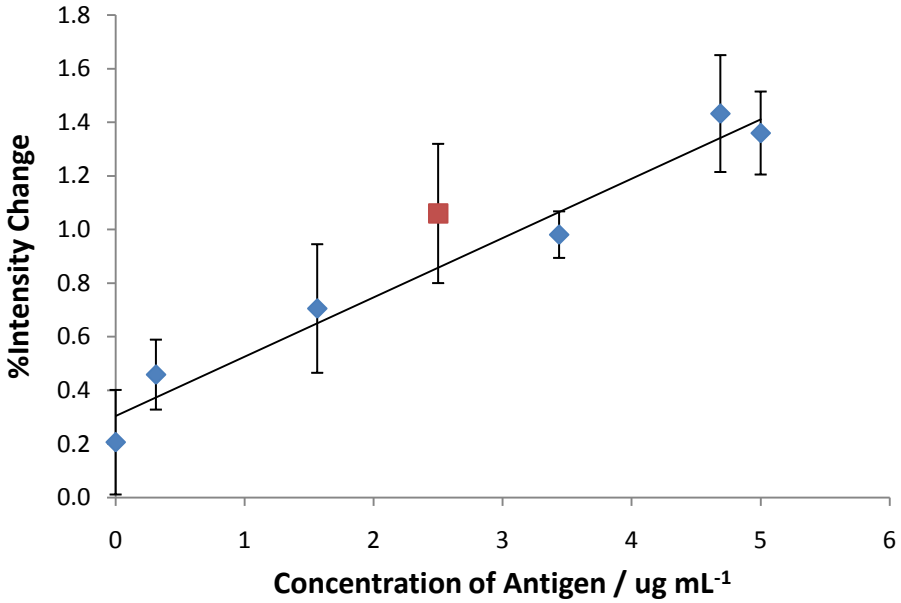

Figure 4-16: Calibration curve for HE4 analysis, obtained using the Sample 2 with the dilution chip and the imagine SPR setup. The diamonds represent the average intensities from all arrays in one channel. The square is the intensity of the solution run through the sample lane. This solution had a nominal concentration of 2.5 µg/mL.

4.6.2.5 Summary

A short summary is shown in

Table 4-2. The lower detection limit of the nanoarray was approximately 1.76 µg/mL. Similar to Biacore technique, there was only 1 antibody needed in order to detect the signal. The total time required to perform an experiment was around 1 day. The human work required were solution preparation and PDMS making. In our setup, we have the advantage of multiplexing and connecting kinetic data simultaneously.

Table 4-2: Short summary of nanoarray experiment with HE4 biomarker.

Nanohole	**Result**
Detection limit	~1.76 μg/mL
Antibody needed	1
Time needed	1 day
Gold chips	Multiple usage
Solution needed	Relatively smaller (than ELISA)
Human works required	Solution preparing + PDMS making
Biggest advantage	Multiplex -multiple concentration -multiple antibodies/antigens

Chapter 5: Determination of the Affinity Constant of the HE4 – HE4 Antibody System

In this chapter, the basic binding kinetic will be introduced and adapted to surface binding kinetics. The approximations considered in our experiment will also be presented and their validity discussed. At the end, the rate constants for adsorption and desorption, k_{on} and k_{off}, respectively, for the binding of HE4 protein on immobilized HE4 antibody were calculated from the data obtain using the nanohole array and the dilution chip nanoarray presented in Chapter 4.

5.1 Binding Kinetics

First, we will consider a binding equilibrium equation, as shown below:

$$A + B \underset{k_d}{\overset{k_a}{\rightleftharpoons}} AB \tag{5-1}$$

In the equation 5-1, molecule A combines with molecule B and form molecule AB. Where k_a represents association rate constant and k_d represents dissociation rate constant. Based on equation 5-1, we can write the general rate equation as equation 5-2[63].

$$-\frac{d[A]}{dt} = -\frac{d[B]}{dt} = \frac{d[AB]}{dt} = k_a[A][B] - k_d[AB] \tag{5-2}$$

If one consider a relaxation experiment with a small perturbation around the equilibrium, the concentration of A, B, and AB can be expressed as equation 5-3(a,b,c)[63].

$$[A] = [A]_e + \Delta A \tag{5-3a}$$

$$[B] = [B]_e + \Delta B \tag{5-3b}$$

$$[AB] = [AB]_e + \Delta AB \quad (5\text{-}3c)$$

Where $[A]_e$, $[B]_e$, and $[AB]_e$ represent the concentrations of A, B, and AB in the equilibrium condition and ΔA, ΔB, and ΔAB represent small changes in concentrations after the perturbation. Also, ΔA, ΔB, and ΔAB are related according to equation 5-4.

$$\Delta A = \Delta B = -\Delta AB \quad (5\text{-}4)$$

Hence, equation 5-5 can be rewritten as[63]:

$$\frac{d[AB]}{dt} = \frac{d([AB]_e + \Delta AB)}{dt} = \frac{d[AB]_e}{dt} + \frac{d\Delta AB}{dt} = \frac{d\Delta AB}{dt} \quad (5\text{-}5)$$

Since $\frac{d[AB]_e}{dt}$ = 0. Therefore, equation 5-2 can be written as below.

$$\frac{d\Delta AB}{dt} = k_a([A]_e + \Delta A)([B]_e + \Delta B) - k_d([AB]_e + \Delta AB) \quad (5\text{-}6)$$

When equation 5-6 is expanded and simplified, the following equation will be obtained.

$$\frac{d\Delta AB}{dt} = k_a[A]_e[B]_e - k_d[AB]_e + k_a(\Delta AB)^2 + [k_a([A]_e + [B]_e) - k_d]\Delta AB \quad (5\text{-}7)$$

At equilibrium,

$$\frac{d[AB]}{dt} = k_a[A]_e[B]_e - k_d[AB]_e = 0 \quad (5\text{-}8)$$

In small perturbation,

$$\Delta AB \ll [A]_e, [B]_e, or\ [AB]_e \quad (5\text{-}9)$$

Thus, the equation 5-7 can be further simplified as below.

$$\frac{d\Delta AB}{dt} = [k_a([A]_e + [B]_e) - k_d]\Delta AB \quad (5\text{-}10)$$

Defining 1/τ as:

$$\frac{1}{\tau} = k_a([A]_e + [B]_e) - \ k_d \tag{5-11}$$

Then, equation 5-10 can be rewritten as:

$$\frac{d\Delta AB}{dt} = \frac{1}{\tau}\Delta AB \tag{5-12}$$

When equation 5-12 is reorganized and integrated[63],

$$\int_{\Delta AB_0}^{\Delta AB} \frac{1}{\Delta AB} d\Delta AB = \frac{1}{\tau}\int_0^t dt \tag{5-13}$$

It result as

$$\ln\left(\frac{\Delta AB}{\Delta AB_0}\right) = \frac{t}{\tau} \tag{5-14}$$

Or

$$\Delta AB = \Delta AB_0 \, e^{\frac{t}{\tau}} \tag{5-15}$$

Substituting equation 5-3c into equation 5-15, yields:

$$[AB] - [\mathrm{AB}]_\mathrm{e} = ([\mathrm{AB}]_0 - [\mathrm{AB}]_\mathrm{e}) \, e^{\frac{t}{\tau}} \tag{5-16}$$

Note $[\mathrm{AB}]_0 = 0$ since we are assuming small perturbation from equilibrium. Therefore, equation 5-16 leads to:

$$[AB] = [\mathrm{AB}]_\mathrm{e}(1 - e^{\frac{t}{\tau}}) \tag{5-17}$$

Similarly, this equation can also be expressed in terms of the reactants A and B, where:

$$\frac{1}{\tau} = k_{obs} = k_a([A]_e + [B]_e) - \ k_d \tag{5-18}$$

5.2 Surface Binding Kinetics

In the previous section, we had discussed the binding kinetics generalized for an A + B system. Now, we are going to apply the same principles into surface adsorption.

$$A_{(aq)}\,(\text{antigen}) + B_{(ad)}\,(\text{antibody}) \underset{k_{off}}{\overset{k_{on}}{\rightleftharpoons}} AB \qquad (5\text{-}19)$$

In equation 5-19, $A_{(aq)}$ represents the antigen solution (aqueous) flown in the channel during the experiments presented in the previous chapters, and $B_{(ad)}$ represents the antibody that is immobilized (adsorbed) in the premodified gold slides. AB represents the complex resulting from the antigen (A) and antibody (B) interaction. k_{on} is the association rate constant and k_{off} represents the dissociation rate constant. In this system, a scheme of the expected plot from a binding kinetics experiment is shown in Figure 5-1.

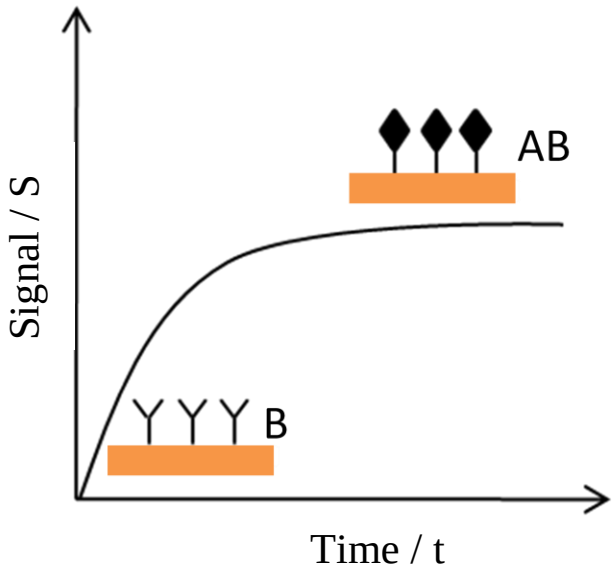

Figure 5-1: Schematic diagram of the expected kinetic graph for a surface binding experiment, as described in equation 5-19.

In Figure 5-1, the antigens are perfectly transported to the surface where they bind to the immobilized antibodies on the gold surface. A signal change (S), proportional to the concentration of AB, is recorded against time (t). The nature of the signal S depends on the experimental arrangement. For example, RU changes or the magnitude of the SPR angle changes are recorded in a typical SPR experiment using the commercial Biacore system. On the other hand, shifts in the resonance wavelength are recorded in a white light transmission setup through nanohole arrays; in this case, changes in the intensities of monochromatic light that matches the resonance wavelength can also be used in the CCD imaging setup (Chapter 4.4.1). Here, we will use intensity changes (*I*) as an example, since this was the sensing mode used to obtain our experimental kinetic data. The surface concentration of AB (Γ_{AB}) is assumed to be directly proportional to the intensity changes *I*:

$$I = \emptyset\, \Gamma_{AB} \tag{5-20}$$

Where $\emptyset$ is just a proportionality factor between the intensity, *I*, and the surface concentration of AB, Γ_{AB}. On the other hands, A is the solution concentration of antibody and the B surface concentration (Γ_B) of "free" adsorbed antigens[64]. Therefore, equation 5-2 can now be written as:

$$\frac{d\Gamma_{AB}}{dt} = k_{on}[A]\Gamma_B - k_{off}\Gamma_{AB} \tag{5-21}$$

The surface concentration (Γ) can also be express as in term of surface coverage (θ), defined as[35]:

$$\theta = \frac{\text{number of AB (occupied sites)}}{\text{total number of sites}} \tag{5-22}$$

Therefore, surface concentration (Γ) can now be written as

$$\Gamma = \Gamma_{\mathrm{m}}\theta \tag{5-23}$$

Where Γ_m represents the maximum surface concentration (all surface adsorption sites are occupied). When this definition is applied into equation 5-21, it turns to:

$$\frac{d\Gamma_{\mathrm{AB}}}{dt} = \Gamma_{\mathrm{m}}(k_{on}[A](1-\theta) - \ k_{off}\theta) \tag{5-24}$$

Using the changes in intensity, as shown in equation 5-20[35,63], we can get:

$$\frac{dI}{dt} = \emptyset\frac{d\Gamma_{\mathrm{AB}}}{dt} = \emptyset\Gamma_{\mathrm{m}}(k_{on}[A](1-\theta) - \ k_{off}\theta) \tag{5-25}$$

Similarly to equation 5-18, the following quantity can be defined:

$$\frac{1}{\tau} = k_{obs} = k_{on}([A]_e + \Gamma_{\mathrm{B}_e}) - \ k_{off} \tag{5-26}$$

5.3 Obtaining k_{on} and k_{off} by Fitting the Exponential Curve

The formalism introduced above allows the rate constants, k_{on} and k_{off}, to be obtained for an affinity experiment performed using SPR. The procedure consists of considering the whole curve and fitting it using the following (simplification equation 5-17).

$$y = a\ (1 - e^{-k_{obs}t}) \tag{5-27}$$

Multiple affinity curves (with different concentration of A) are obtained and fitted to obtain k_{obs}. A plot of k_{obs} against the $[A]_e$ yields k_{on} as the slope and k_{off} as the intercept, as shown in Figure 5-2[63]. (note Γ_{B_e}~ 0 since most of the site are bound at equilibrium)

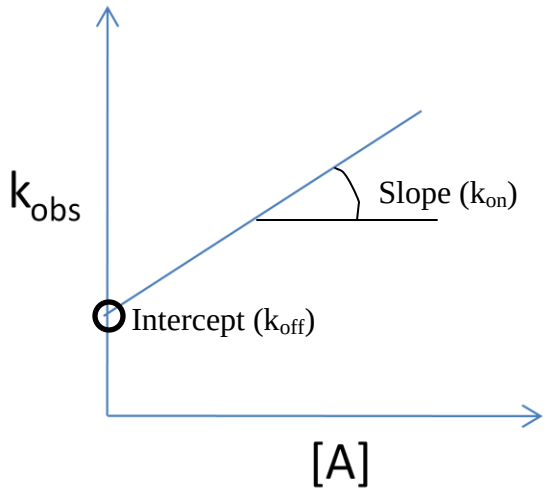

Figure 5-2: Schematic of the expected relationship between k_{obs} and concentration of antigen.

5.4 Obtaining k_{on} with Short time of Kinetic Data

In the previous section, we had shown how to obtain the values of k_{on} and k_{off} from the whole affinity curve. However, in most situations, the time to reach equilibrium is too long and only the initial portion of the adsorption curve (linear portion) is obtained, as illustrated in Figure 5-3.

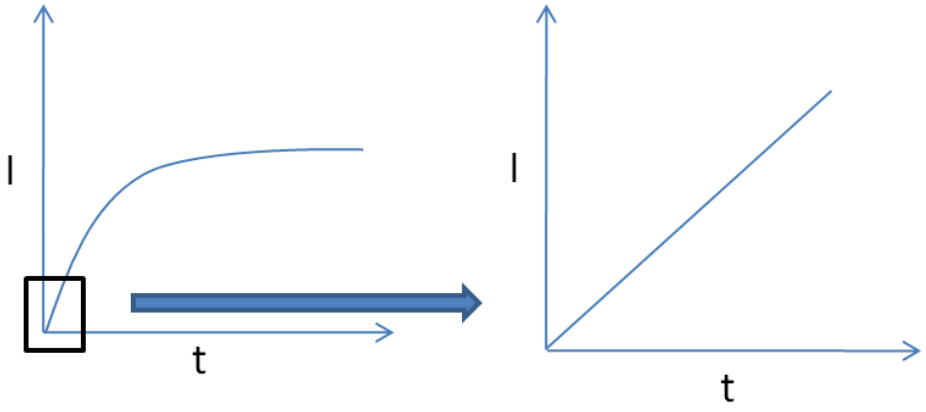

Figure 5-3: Diagram to illustrate the initial time of an affinity kinetic curve.

In this situation, $k_{on}[A] >> k_{off}$ is assumed and $\theta \sim 0$ for short period of time[63]. Now, equation 5-25 can be simplified to:

$$\frac{dI}{dt} = \emptyset\Gamma_m(k_{on}[A]) \quad (5\text{-}28)$$

In this case, plots of the slope of the initial part of the intensity vs. time curves against the concentration of A are obtained.

The slope (S_s) can be expressed as:

$$S_s = (\emptyset\Gamma_m)k_{on} = I_{max}k_{on} \quad (5\text{-}29)$$

Where $\emptyset\Gamma_m$ is equal to maximum intensity (I_{max}), as shown in equation 5-20. A limitation of this approach is that an independent way to estimate the value of I_{max} need to be devised, as illustrated in Figure 5-4.

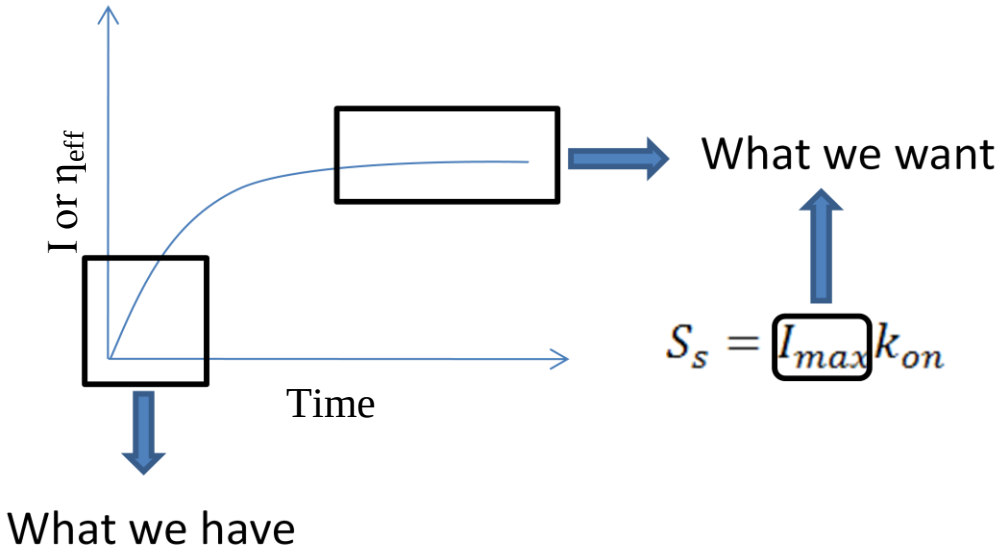

Figure 5-4: Scheme illustrating the problem of estimating I_{max}, which is required to obtain k_{on} from the initial part of the kinetic curve.

Since SPR measures the local refractive index at the surface, the value of I_{max} can be estimated from a simple analysis of the effective refractive index (η_{eff}), as discussed in the next section.

5.5 Estimating Effective Refractive index (η_{eff})

From Chapter 4, we have discussed that the intensity of transmitted light though arrays of nanoholes has a direct relationship with the effective refractive index (η_{eff}) at the metal-solution interface. Effective refractive index (η_{eff}) is defined as the average refractive index in the region within the SPR effective field. This field decays exponentially as the distance further from the gold metal surface, as we mention on section 2.2. On the other hand, refractive index changes closer to the gold surface give greater effect than the same change farther from the gold surface.

Now, we have turned the problem of estimating the maximum intensity into estimating the effective refractive index probed by the SPR field. In order to solve this problem, a modified Campbell and Kim's model[65] was used, as shown in Figure 5-5. In this model, we are assuming a monolayer of antibody of thickness d_{ab} is attached on the gold surface and a monolayer of antigen (of thickness d_{ag}) is bound to the antibody at the end of the binding process (equilibrium situation).

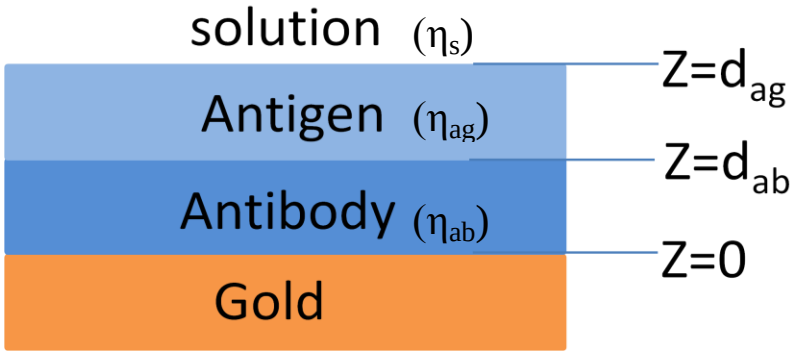

Figure 5-5: Gold surface coated with a layer of antibody, a layer of antigen and in contact to an aqueous solution. The refractive index of each layer is represented as η (η_s, η_{ag}, η_{ab}) and Z represents the distance away from the gold surface with respected as gold surface Z = 0.

The η_{eff} can then be calculated by using the equation 5-30[65].

$$\eta_{eff} = \int_{Z=0}^{Z=\infty} \eta(Z) e^{(\frac{-Z}{h})}\, dZ \qquad (5\text{-}30)$$

The surface plasmon field decays exponentially from the surface towards the dielectric medium (section 2.2). Therefore, not only the refractive index at the surface, but anywhere within this exponential field, will contribute to the changes in the SPR.

When the equation 5-30 is applied into the model shown in Figure 5-5, the following equation is expressed.

$$\eta_{eff} = \int_{Z=0}^{Z=d_{ab}} \eta_{ab} e^{(\frac{-Z}{h})}\, dZ + \int_{Z=d_{ab}}^{Z=d_{ag}} \eta_{ag} e^{(\frac{-Z}{h})}\, dZ + \int_{Z=d_{ag}}^{Z=\infty} \eta_s e^{(\frac{-Z}{h})}\, dZ \qquad (5\text{-}31)$$

After the equation 5-31 is evaluated and simplified, it leads to equation 5-32.

$$\eta_{eff} = \eta_{ab} + (\eta_{ag} - \eta_{ab})[e^{(\frac{-d_{ab}}{h})}] + (\eta_s - \eta_{ag})[e^{(\frac{-d_{ag}}{h})}] \qquad (5\text{-}32)$$

In equation 5-32, η_{ab}, η_{ag}, and η_s are the refractive index of antibody, antigen, and the buffer used. The d_{ab} and d_{ag} are the thickness of the antibody and the antigen layers, respectively. *h* is the decay length of the SPR field into the solution. When the maximum η_{eff} is found, we can track back and calculate the expected maximum intensity change considering total surface saturation. This value will be used to obtain k_{on}.

5.6 Estimating the Maximum Effective Refractive Index using Campbell's Model

For calculating the maximum η_{eff}, the values for η_{ab} and η_{ag} used were both 1.45 which is a typical refractive index for proteins[66]. The η_s value used was 1.3327, which is the refractive index of PBS buffer measured with a refractometer. Lambda (λ) was 200 nm, which is a typical decay length for a surface plasmon resonance. For d_{ab} and d_{ag}, it was assumed that a monolayer of antibody and a monolayer of antigen on the top of the gold surface were formed. Within this assumption, d_{ab} is the diameter of the antibody and d_{ag} is the diameter of the antibody + antigen. The individual diameters for both the antibody and the antigen are estimated by equation 5-33[67].

$$MW = (\alpha r)^{\beta} \tag{5-33}$$

Where MW is the molecular weight of the proteins (antibody or antigen) in ($x10^3$) a.m.u.; α and β are the correction factors equal to 1.68 and 2.3398, respectively and r represents the radius of the protein molecules in nm. The molecular weight of the antibody used was 150,000 a.m.u. and the antigen was 11,000 a.m.u. Therefore, the calculated radius for the antibody and antigen were 5.07 nm and 1.66 nm respectly.

5.7 Obtaining Maximum Intensity by Fitting Refractive Index into Glucose Calibration Curve

After the maximum η_{eff} was calculated, the value was fitted into the calibration line obtained from experiments with glucose solutions of known refractive indexes, as shown in Figure 5-6, and the maximum % intensity changed was estimated.

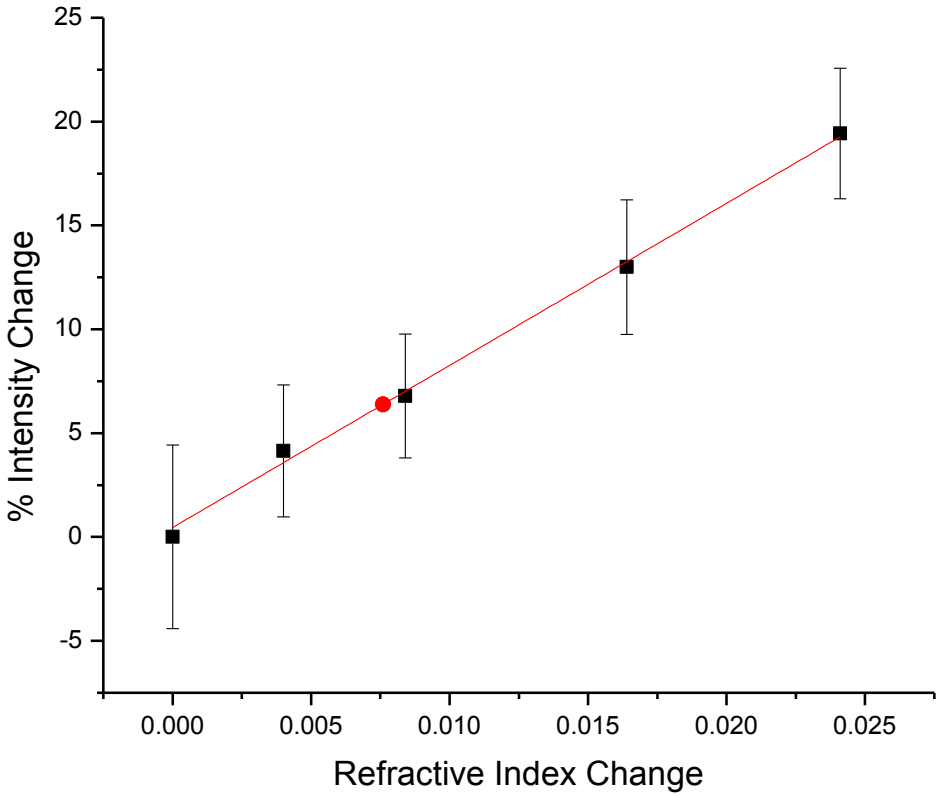

Figure 5-6: Glucose calibration line (note: this is identical graph to Figure 4-13 with correction of water signal to 0 and the x-axis to changing in refractive index). The red circle dot is the calculated value of max η_{eff} as discussed.

5.8 Calculating k_{on} from the Maximum Intensity Found from Estimation

After the maximum change in intensity (expected when the surface is completely saturated by the adsorption of the antigen) was calculated, this value was put into the equation 5-29. As shown in the equation 5-29, the k_{on} value was calculated by the slope (of the plot S_s vs. the concentration of antigen, presented in Figure 5-7) divided by the maximum intensity. In Figure 5-7, a negative slope was obtained because we have decreasing values in intensity due to adsorption, as discussed in section 4.4. In the calculation, the absolute value of the slope was used. The k_{on} of HE4 obtained was (10 ± 2) x 10^4 $M^{-1}s^{-1}$.

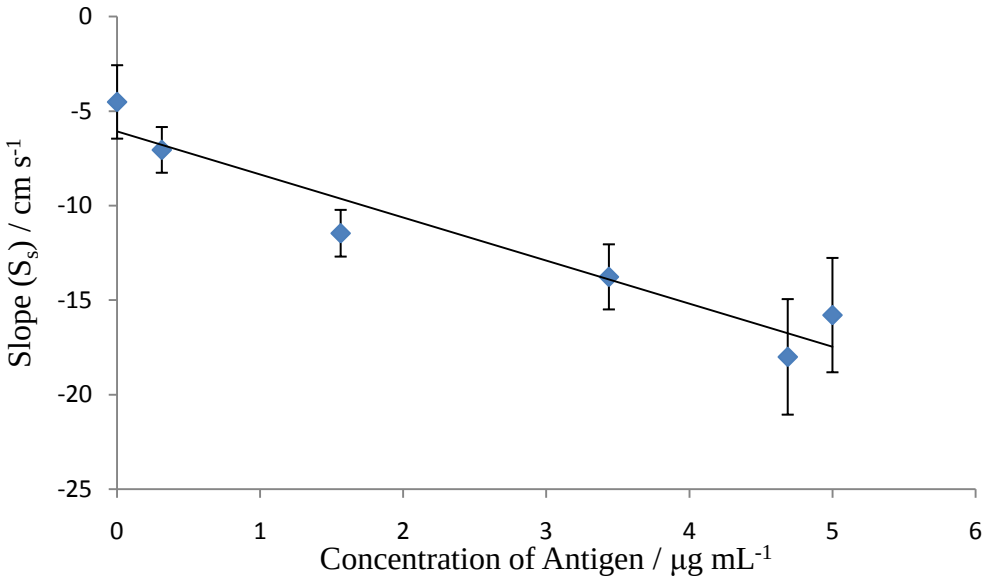

Figure 5-7: Relationship between slope of kinetic curve (equation 5-29) and the concentration of the HE4 antigens.

5.9 Calculating k_{off} by Fitting the Exponential Decay Curve

The k_{off} value was obtained by fitting equation 5-27 into the curve obtained after flushing the channels with PBS (Figure 5-8). In this case, the concentration of A ~ 0 and the k_{obs} is equal to k_{off} (equation 5-26). The average k_{off} obtained was $(2.2 \pm 1.0) \times 10^{-3}$ s^{-1}. The average value was the average for all arrays (24 arrays) among different concentrations. Although the value of k_{off} varies from array by arrays, the order of the k_{off} were very close to each other (~10^{-3}). Figure 5-8 shows that the k_{off} value for different concentrations of antigens did not follow the trend as what we expected since the k_{off} should be simple equal to k_{obs} in our case. The errors were the standard deviation of all arrays.

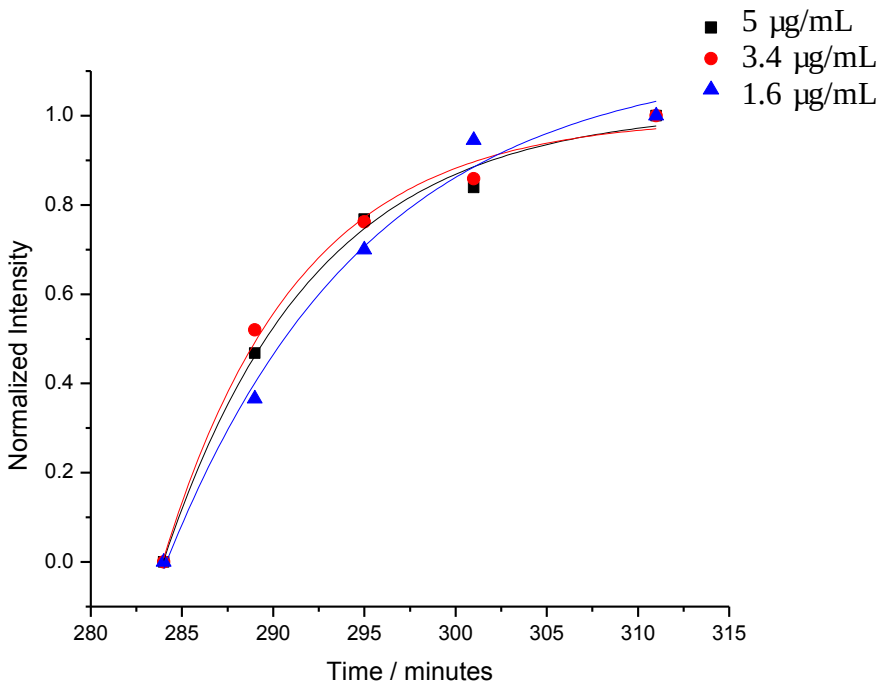

Figure 5-8: k_{off} fitting curve on exponential equation (Sample array data for array with different concentrations of antigen flown).

The equilibrium constant (K) which is defined as k_{on}/k_{off} was $(4.3 \pm 2.1) \times 10^7\ M^{-1}$. This value agrees well with the typical values obtained from other protein binding systems which is in the range between $(1x10^7 \sim 1x10^{11})$[68].

Chapter 6: Conclusion

In this thesis, we had compared the advantages and disadvantages of different analytical platforms (ELISA, Biacore, and Nanohole arrays) for the analysis of the ovarian cancer marker HE4. The short summary of the comparison is presented in Table 6-1. In the table, we can conclude that the biggest advantage for ELISA is it has the lowest detection limit among the method used. Both SPR based platforms, using the Biacore instrument or the arrays of Nanoholes, have advantages of being a label free detection (only 1 antibody needed), more environmental friendly (multiple sensor used, less waste of solvent), and provided information regarding real time measurement for protein binding. The biggest advantage of the nanohole-based sensing over the commercial Biacore system was that the nanohole imaging SPR allows multiple samples to be analyzed simultaneously and in real time. This multiplexing advantage can be further explored to detect multiple biomarkers (with alternative design of PDMS channel) using a single chip, leading us one step closer to our final goal. Also, we estimated the equilibrium constant for HE4 antibody and antigen pair using arrays of nanoholes with Campbell's model. The constant can then help us on determining the best antibody and antigen pair. As we mention in chapter 2.5.2, the main use for Biacore in the BCCA is to determine the best pair of antibody and antigen. By using Biacore, the time saved from this process varies from weeks/months to few days. With the advantage of the nanohole technique on the multiplex, it is possible to reduce the analysis time even further.

Table 6-1: Summary of advantages and disadvantage for ELISA, Biacore, and Nanohole.

	ELISA	Biacore	Nanohole
Detection limit	~0.5 ng/mL	~0.13 μg/mL	~1.76μg/mL
Time used	1 day	1 day	1 day
Plates/Chips	Single	Multiple	Multiple
Antibody needed	2	1	1
Solution needed	Largest	Less	Less
Biggest Advantage	Lowest detection limit	Real time Measurement	Multiplex

Bibliography

(1) Littrup, P. J.; Kane, R. A.; Mettlin, C. J.; Murphy, G. P.; Lee, F.; Toi, A.; Badalament, R.; Babaian, R. *Cancer* **1994**, *74*, 3146-3158.

(2) Rahman M, I. N., Roblyer D, Stepanek V, Richards-Kortum R, Gillenwater A, Shastri S, Chaturvedi P *Head & Neck Oncology* **2010**, *2*, 10.

(3) Wang, J. *Biosensors and Bioelectronics* **2006**, *21*, 1887-1892.

(4) Khandurina, J.; Guttman, A. *Journal of Chromatography A* **2002**, *943*, 159-183.

(5) Choi, J.-W.; Oh, K. W.; Thomas, J. H.; Heineman, W. R.; Halsall, H. B.; Nevin, J. H.; Helmicki, A. J.; Henderson, H. T.; Ahn, C. H. *Lab on a Chip* **2002**, *2*, 27-30.

(6) Oleschuk, R. D.; Shultz-Lockyear, L. L.; Ning, Y.; Harrison, D. J. *Analytical Chemistry* **1999**, *72*, 585-590.

(7) Daniel, L. *The New Engliand Journal of Medicine* **2009**, *361*, 170-177.

(8) Brolo, A. G.; Gordon, R.; Leathem, B.; Kavanagh, K. L. *Langmuir* **2004**, *20*, 4813-4815.

(9) Brolo, A. G.; Arctander, E.; Gordon, R.; Leathem, B.; Kavanagh, K. L. *Nano Letters* **2004**, *4*, 2015-2018.

(10) De Leebeeck, A.; Kumar, L. K. S.; de Lange, V.; Sinton, D.; Gordon, R.; Brolo, A. G. *Analytical Chemistry* **2007**, *79*, 4094-4100.

(11) Sinton, D.; Gordon, R.; Brolo, A. *Microfluidics and Nanofluidics* **2008**, *4*, 107-116.

(12) Gordon, R.; Brolo, A. G.; Kavanagh, K. L. *Accounts of Chemical Research* **2008**, *41*, 1049-1057.

(13) Ferreira, J.; Santos, M. J. L.; Rahman, M. M.; Brolo, A. G.; Gordon, R.; Sinton, D.; Girotto, E. M. *Journal of the American Chemical Society* **2008**, *131*, 436-437.

(14) Eftekhari, F.; Escobedo, C.; Ferreira, J.; Duan, X.; Girotto, E. M.; Brolo, A. G.; Gordon, R.; Sinton, D. *Analytical Chemistry* **2009**, *81*, 4308-4311.

(15) Gordon, R.; Brolo, A.; Sinton, D.; Kavanagh, K. *Laser & Photonics Reviews*, *4*, 311-335.

(16) Cannistra, S. A. *New England Journal of Medicine* **2004**, *351*, 2519-2529.

(17) Jemal, A.; Siegel, R.; Xu, J.; Ward, E. *CA: A Cancer Journal for Clinicians* **2010**, caac.20073.

(18) Palmer, C.; Duan, X.; Hawley, S.; Scholler, N.; Thorpe, J. D.; Sahota, R. A.; Wong, M. Q.; Wray, A.; Bergan, L. A.; Drescher, C. W.; McIntosh, M. W.; Brown, P. O.; Nelson, B. H.; Urban, N. *PLoS ONE* **2008**, *3*, e2633.

(19) Gupta, D.; Lis, C. *Journal of Ovarian Research* **2009**, *2*, 13.

(20) Ian, J. J.; Steven, J. S.; Nicola, M.; Usha, M.; Adam, N. R.; Ann Prys, D.; Robert, W.; Arjun, R. J.; Karen, S.; David, G. L.; David, H. O. *LANCET* **1999**, *353*, 1207-1210.

(21) Domar, A. D. *Women & Health* **1986**, *10*, 75-90.

(22) Tyronne, I. G.; Marcia, R. H.; Gordon, J. S. R. *LANONC* **2007**, *8*, 813-821.

(23) Network, N. C. C.; National Comprehensive Cancer Network: 2009; Vol. v2.

(24) Bast, R. C.; Xu, F. J.; Yu, Y. H.; Barnhill, S.; Zhang, Z.; Mills, G. B. *The International journal of biological markers* **1998**, *13*, 179-187.

(25) Bagan, P.; Berna, P.; Assouad, J.; Hupertan, V.; Le Piepec Barthes, F.; Riquet, M. *The European respiratory journal* **2008**, *31*, 140-142.

(26) Bast, R. C.; Feeney, M.; Lazarus, H.; Nadler, L. M.; Colvin, R. B.; Knapp, R. C. *The Journal of Clinical Investigation* **1981**, *68*, 1331-1337.

(27) Havrilesky, L. J.; Sanders, G. D.; Kulasingam, S.; Myers, E. R. *Gynecologic Oncology* **2008**, *111*, 179-187.

(28) Tchagang, A. B.; Tewfik, A. H.; DeRycke, M. S.; Skubitz, K. M.; Skubitz, A. P. N. *Molecular Cancer Therapeutics* **2008**, *7*, 27-37.

(29) Huhtinen, K.; Suvitie, P.; Hiissa, J.; Junnila, J.; Huvila, J.; Kujari, H.; Setala, M.; Harkki, P.; Jalkanen, J.; Fraser, J.; Makinen, J.; Auranen, A.; Poutanen, M.; Perheentupa, A. *British Journal of Cancer* **2009**, *100*, 1315-1319.

(30) Bingle, L.; Singleton, V.; Bingle, C. D. *Oncogene* **2002**, *21*, 2768-2773.

(31) Wood, R. W. *Proceedings of the Physical Society of London* **1902**, *18*, 269.

(32) Fano, U. *Journal of the Optical Society of America* **1941**, *31*, 213-222.

(33) Otto, A. *Zeitschrift für Physik A Hadrons and Nuclei* **1968**, *216*, 398-410.

(34) Kretschmann, E. *Optics Communications* **1972**, *6*, 185-187.

(35) Somorjai, G. A.; Li, Y. *Introduction to Surface Chemistry and Catalysis*; John Wiley & Sons, Lnc.: New Jersey, 2010.

(36) Neumann, T.; Junker, H. D.; Schmidt, K.; Sekul, R. *Current Topics in Medicinal Chemistry* **2007**, *7*, 1630-1642.

(37) Homola, J. *Chemical Reviews* **2008**, *108*, 462-493.

(38) www.biacore.com

(39) Myszka, D. G. In *Methods in Enzymology*; Academic Press: 2000; Vol. Volume 323, p 325-340.

(40) Schröter, U.; Heitmann, D. *Physical Review B* **1999**, *60*, 4992-4999.

(41) Raether, H. *Surface Plasmons on Smooth and Rough Surfaces and on Gratings*; Springer-Verlag: New York, 1986.

(42) El-Brolossy, T. A.; Abdallah, T.; Mohamed, M. B.; Abdallah, S.; Easawi, K.; Negm, S.; Talaat, H. *European Physical Journal Special Topics* **2008**, *153*, 361-364.

(43) Kocabas, A.; Dana, A.; Aydinli, A. *Applied Physics Letters* **2006**, *89*, 041123.

(44) García de Abajo, F. J.; Gómez-Medina, R.; Sáenz, J. J. *Physical Review E* **2005**, *72*, 016608.

(45) Barnes, W. L.; Dereux, A.; Ebbesen, T. W. *Nature* **2003**, *424*, 824-830.

(46) Coe, J. V.; Rodriguez, K. R.; Teeters-Kennedy, S.; Cilwa, K.; Heer, J.; Tian, H.; Williams, S. M. *The Journal of Physical Chemistry C* **2007**, *111*, 17459-17472.

(47) Lesuffleur, A.; Im, H.; Lindquist, N. C.; Lim, K. S.; Oh, S.-H. *Proceedings of SPIE* **2008**, *7035*, 703504-1-703504-10.

(48) Marx, U.; Embleton, M. J.; Fischer, R.; Gruber, F. P.; Hansson, U.; Heuer, J.; de Leeuw, W. A.; Logtenberg, T.; Merz, W.; Portetelle, D.; Romette, J. L.; Straughan, D. W. *ATLA* **1997**, 121-137.

(49) Butler, J. E. *Journal of Immunoassay* **2000**, *21*, 165-209.

(50) Ma, H.; Shieh, K. J.; Lee, S. L. *Nature and Science* **2006**, *4*, 36-37.

(51) Quinn, J. G.; O'Neill, S.; Doyle, A.; McAtamney, C.; Diamond, D.; MacCraith, B. D.; O'Kennedy, R. *Analytical Biochemistry* **2000**, *281*, 135-143.

(52) Rich, R. L.; Myszka, D. G. *Drug Discovery Today: Technologies* **2004**, *1*, 301-308.

(53) Fivash, M.; Towler, E. M.; Fisher, R. J. *Current Opinion in Biotechnology* **1998**, *9*, 97-101.

(54) Myszka, D. G.; Jonsen, M. D.; Graves, B. J. *Analytical Biochemistry* **1998**, *265*, 326-330.

(55) Malmborg, A.-C.; Borrebaeck, C. A. K. *Journal of Immunological Methods* **1995**, *183*, 7-13.

(56) Wood, S. J. *Microchemical Journal* **1993**, *47*, 330-337.

(57) Skoog, D. A.; Holler, J., F. J.; Crouch, S. R. *Principles of Instrumental Analysis*; 6 ed.; Thomson Corporation: Belmont, 2007.

(58) Ng, J. M. K.; Gitlin, I.; Stroock, A. D.; Whitesides, G. M. *ELECTROPHORESIS* **2002**, *23*, 3461-3473.

(59) Kim, C.; Lee, K.; Kim, J. H.; Shin, K. S.; Lee, K.-J.; Kim, T. S.; Kang, J. Y. *Lab on a Chip* **2008**, *8*, 473-479.

(60) Irima, D.; Geba, D. A.; Toner, M. *Analytical Chemistry* **2006**, *78*, 3472-3477.

(61) Gordon, R.; Brolo, A. G.; Kavanagh, K. L. *Lasers and Photonics Reviews* **2010**, *4*, 311-335.

(62) Gonzalez, M.; Bagatolli, L. A.; Echabe, I.; Arrondo, J. L. R.; Argarana, C. E.; Cantor, C. R.; Fidelio, G. D. *The Journal of Biological Chemistry* **1997**, *272*, 11288-11294.

(63) Bernasconi, C. F. *RELAXATION KINETICS*; Academic Press, Lnc.: New York, 1976.

(64) Lyons, M. E. G. *Sensors* **2001**, *1*, 215-228.

(65) Campbell, C. T.; Kim, G. *Biomaterials* **2007**, *28*, 2380-2392.

(66) Beketov, G. V.; Shirshov, Y. M.; Shynkarenko, O. V.; Chegel, V. I. *Sensors and Actuators B: Chemical* **1998**, *48*, 432-438.

(67) Zhelev, N.; Barudov, S. *Biotechnology & Biotechnological Equipment* **2005**, 19/2005/3.

(68) Zhang, J.; Kinsel, G. R. *Langmuir* **2003**, *19*, 3531-3534.